Chemical Engineering Research and Design 212 (2024) 493–519

Contents lists available at ScienceDirect

Chemical Engineering Research and Design

journal homepage: www.elsevier.com/locate/cherd

Modeling and control of a protonic membrane steam methane reformer

Xiaodong Cui [a,1], Dominic Peters [a,1], Yifei Wang [a], Berkay Çıtmacı [a], Derek Richard [a], Carlos G. Morales-Guio [a,*], Panagiotis D. Christofides [a,b,**]

[a] Department of Chemical and Biomolecular Engineering, University of California, Los Angeles, CA, 90095-1592, USA
[b] Department of Electrical and Computer Engineering, University of California, Los Angeles, CA 90095-1592, USA

ARTICLE INFO

Keywords:
Decentralized model predictive control (DMPC)
Protonic membrane reformer (PMR)
Steam methane reforming
Disturbance observer (DOB)
Lumped parameter modeling
Adaptive control

ABSTRACT

Steam methane reforming in solid oxide proton conducting membranes is a state-of-the-art process capable of initiating methane reforming reactions, electrochemical hydrogen separation, and the compression of purified hydrogen product within a single electrochemical processing unit. Given the many process variables involved, a model predictive controller is needed to safely operate a protonic membrane reformer (PMR) under dynamic operational conditions by employing physically relevant constraints that protect the reactor materials of construction and maximize the stability of the process. This work derives, and experimentally validates, physics-based models for a PMR process and integrates an overall process model into centralized and decentralized model predictive control schemes. The performance of control actions from classical proportional–integral controllers and model predictive controllers are surveyed, and the decentralized model predictive control algorithm, developed here, obeys practical constraints, reaches the target variables' setpoints quickly, and lowers computational costs relative to the centralized predictive controller. Finally, the addition of a disturbance observer (DOB) ensures robust controller performance when subject to incomplete and infrequent process measurements or common system disturbances.

1. Introduction

From bench-scale to commercial-scale process intensification efforts, the operation of novel chemical process designs involves controlling predictable and stochastic subprocesses that must be modeled with some combination of theory and data. For high-temperature electrocatalysis, which generally describes any steam methane reforming (SMR) process in solid oxide proton conducting membranes, straightforward analytical models can be derived from reaction engineering first principles. The challenge of employing such models within control schemes arises from the physical and chemical instability of catalysts in extreme reactor conditions, given the surface chemistry of these catalysts is in rapid flux as a result of the large thermal and electrochemical forces applied (Yuste-Tirados et al., 2024). Additional complexity, in terms of kinetic modeling, is introduced from the stochastic nature of catalyst deactivation, coupled with hard-to-measure thermal and electrochemical side reactions that are responsible for oxidizing catalytically active surface sites in the anodic electrode of a protonic membrane reformer (Jang et al., 2024). Consequently, each test of an electrified methane reforming system yields varying degrees of catalyst deactivation that materializes through a variety of physical and chemical mechanisms at random times. Additionally, the resistance of the solid electrolyte membrane, responsible for facilitating the electrochemical separation of hydrogen from anode to cathode (Yuste-Tirados et al., 2023), rapidly fluctuates and causes an unsteady heat flux through the body of the membrane and to the reactants. Therefore, novel electrified SMR processes in solid oxide proton conducting membranes require sophisticated control schemes regulated by physically relevant operational constraints.

Traditional control schemes like proportional–integral–derivative (PID) control are widely used for their algorithmic simplicity and their reliability in maintaining the safe, steady state operation of process systems. However, these control schemes exhibit limitations when applied to complex systems characterized by nonlinear dynamics, multi-variable interactions, and controller response speed. These limitations become significant in advanced chemical processing systems like novel electrified SMR reactors, where sudden changes in reaction states, stringent operational limits, and complex physical and chemical mechanisms make optimal control of such reactor systems very challenging.

* Corresponding author.
** Corresponding author at: Department of Chemical and Biomolecular Engineering, University of California, Los Angeles, CA, 90095-1592, USA.
E-mail addresses: moralesguio@ucla.edu (C.G. Morales-Guio), pdc@seas.ucla.edu (P.D. Christofides).
[1] These authors contributed equally.

https://doi.org/10.1016/j.cherd.2024.11.006
Received 12 October 2024; Received in revised form 3 November 2024; Accepted 4 November 2024
Available online 21 November 2024

Model predictive control (MPC), by contrast, regulates process variability in complex systems by predicting future mass and energy states based on dynamic models of the overall system structure. This advanced controller can also optimize control input actions according to induced setpoint changes and unpredictable system disturbances. Our previous work demonstrated the dynamic modeling and MPC of an electrified SMR system, in contrast to most of the existing research, which focuses on conventional fire-heated SMR systems. For example, Cui et al. (2024) and Çıtmacı et al. (2024) synthesized a physics-based, lumped-parameter model for an electrically heated SMR system and integrated the model into a model predictive controller using an extended Luenburger observer. In Wang et al. (2024), a recurrent neural network model was developed for an electrically heated SMR system and integrated into an MPC scheme with an integrator and offset-free MPC, both of which showed enhanced control behavior compared to proportional–integral (PI) controllers. An online machine learning model would most likely require re-training and could introduce uncertainty into the control action calculation process, especially for operational conditions and phenomena not captured in training data sets. Given steam methane reforming processes can accurately be described by reaction engineering-based first-principles models, there is no need to introduce a less reliable machine learning model into the MPC algorithm. For reactors with kinetics that are not well-understood, a machine learning approach to modeling would be more suitable. Thus, in this work, we advance the field by implementing a multi-input–multi-output (MIMO) MPC scheme in a PMR to manage the complex phenomena of the system using first-principles modeling techniques. For SMR processes in solid oxide proton conducting membranes, specifically, MPC adapts to rapid changes in electrode surface chemistry, allowing the controller to adjust inputs in real time, reducing the impact of unforeseen flow and temperature variations that would otherwise forfeit the stability of the system.

The implementation of MPC requires full-state measurement feedback at each sampling time. However, in many chemical processes, not all system states are directly measurable (Soroush, 1997). Even if a particular system state can be measured, the detection of that state may be infrequent. This situation necessitates the use of a state observer. Additionally, the MPC model may become inaccurate due to disturbances originating from thermal fluctuations, electrochemical side reactions, or catalyst degradation. To address these issues, an observer is integrated into a predictive controller to estimate unmeasured system states and to correct model predictions in real time. This correction is crucial as it allows the controller to compensate for different physical disturbances, such as unsteady heat flux and varying electrode resistance, that directly impact the final state of the PMR system. By using a disturbance observer (DOB), the MPC scheme maintains robust and precise control over key target variables, mainly, the rate of pure H_2 generation.

To address the computational challenges of implementing MPC in a real chemical process, a decentralized model predictive control (DMPC) strategy is employed. By dividing the system into smaller, decoupled subsystems with independent controllers, DMPC significantly reduces the computational load of the controller while maintaining system-wide coordination (Bemporad and Barcelli, 2010; Richards and How, 2004; Chen et al., 2020). Each local controller manages specific process constraints, allowing for faster optimization calculations and real time adjustments. As a result, this decentralized approach enables scalable control, making it feasible for commercial-scale SMR control applications that do not compromise system performance or the hydrogen production capacity of a PMR.

2. Preliminaries

2.1. Notation

The symbol $\|\cdot\|$ represents the Euclidean norm of a vector. The transpose of vector $\boldsymbol{x}$ is denoted by $\boldsymbol{x}^\top$. $\mathbb{R}$ represents the set of real numbers. A function, $f(\cdot)$, falls under the class C^1 if it is continuously differentiable within its defined domain.

Definitions of variables used in the modeling of the reactor and bubbler:

- A_h, A_h^r, A_h^p, $A_h^{a,PMR}$, $A_h^{c,PMR}$, A_h^b: Surface area for heat loss, of retentate, of permeate, of PMR anode, of PMR cathode, of bubbler [m^2].
- A_i: Pre-exponential factor of adsorption constant K_i [Pa^{-1} for $i = CH_4, H_2, CO$ and unitless for $i = H_2O$].
- A_j: Pre-exponential factor of rate coefficient k_i [mol $Pa^{0.5}$ (kg_{cat} s)$^{-1}$ for $j = 1$ (SMR reaction), mol (Pa kg_{cat} s)$^{-1}$ for $j = 2$ (WGS reaction)].
- C_i, C_i^r, C_i^p, $C_i^{a,PMR}$, $C_i^{c,PMR}$: Concentration of gas i, in retentate, in permeate, in PMR anode, in PMR cathode [mol m^{-3}].
- $C_{p,i}$: Heat capacity of species i [J (kg K)$^{-1}$].
- E_j: Activation energy of reaction j [J mol^{-1}].
- $F_{i,0}$, $F_{i,0}^r$, $F_{i,0}^p$, $F_{i,0}^{a,PMR}$, $F_{i,0}^{c,PMR}$, $F_{i,0}^b$: Inlet molar flowrate of gas i, of retentate, of permeate, of PMR anode, of PMR cathode, of bubbler [mol s^{-1}].
- $F_{k,rem}$: Removal rate of gas k [mol s^{-1}].
- I_m, I_f: Current through membrane, current to heat furnace [A].
- K_i: Adsorption constant of gas i [Pa^{-1} for $i = CH_4, H_2, CO$ and unitless for $i = H_2O$]
- K_j: Equilibrium constant of reaction j [Pa^2 for $j = 1$ (SMR reaction), unitless for $j = 2$ (WGS reaction)]
- k_j: Reaction rate constant of reaction j [mol $Pa^{0.5}$ (kg_{cat} s)$^{-1}$ for $j = 1$ (SMR reaction), mol (Pa kg_{cat} s)$^{-1}$ for $j = 2$ (WGS reaction)]
- M_{H_2O}: Molecular mass of H_2O [kg mol^{-1}]
- P, P^r, P^p, $P^{a,PMR}$, $P^{c,PMR}$, P^b: Pressure, of retentate, of permeate, of PMR anode, of PMR cathode, of bubbler [Pa]
- P_i: Partial pressure of gas i [Pa]
- q, q^r, q^p, $q^{a,PMR}$, $q^{c,PMR}$: Outlet volumetric flowrate, of retentate, of permeate, of PMR anode, of PMR cathode [m^3 s^{-1}].
- r_j: Rate of reaction j per kilogram of catalyst [mol (kg s)$^{-1}$].
- R_j: Rate of reaction j [mol s^{-1}].
- R: Universal gas constant [J (mol K)$^{-1}$]
- R_f, R_m: Electric resistance of furnace, of membrane [Ω].
- $R_{i,gen}$: Generation rate of species i due to reaction [mol s^{-1}].
- T, T^a, T^r, T^p, $T^{a,PMR}$, $T^{c,PMR}$: Temperature, of ambient, of retentate, of permeate, of PMR anode, of PMR cathode [K].
- T_0, T_0^r, T_0^p, T_0^b: Temperature at the inlet, of retentate, of permeate, bubbler [K].

- U_h, U_h^r, U_h^p, $U_h^{a,PMR}$, $U_h^{c,PMR}$, U_h^b: Overall heat transfer coefficient, of retentate, of permeate, of PMR anode, of PMR cathode, of bubbler [J (s K m^2)$^{-1}$]
- V, V^r, V^p, V_{gas}^b, V^b: Volume of reactor, of retentate, of permeate, of gas in bubbler, of bubbler [m^3]
- W_{cat}: Weight of catalyst [kg]
- ΔH_{r_j}: Enthalpy change of reaction j [J mol^{-1}]
- ρ_i, ρ_i^r, ρ_i^p, ρ_i^b: Density of species i, of retentate, of permeate, of bubbler [kg m^{-3}]

2.2. Class of systems

A general nonlinear system is described by the following equations:

$$\dot{\boldsymbol{x}} = \boldsymbol{F}(\boldsymbol{x}, \boldsymbol{u}) \tag{1a}$$

$$\boldsymbol{y} = \boldsymbol{h}(\boldsymbol{x}, \boldsymbol{u}) \tag{1b}$$

where the state vector is denoted by $\boldsymbol{x} \in \mathbb{R}^n$, and $\boldsymbol{u} \in \mathbb{R}^m$ represents the manipulated (control) input vector, constrained by the set $U \subset \mathbb{R}^m$. $\boldsymbol{y} \in \mathbb{R}^k$ is the measured (to be controlled) output vector. $\boldsymbol{F} \in \mathbb{R}^n$ represents a general nonlinear vector function and is used to represent a typically unknown process model. Without loss of generality, we assume the initial time to be zero ($t_0 = 0$).

We consider $j = 1, \dots, N_{sys}$ subsystems, where each subsystem j is regulated by its respective control input u_j and can be influenced by interactions with other subsystems due to coupling effects. The continuous-time nonlinear dynamics for each subsystem j are given by:

$$\dot{\boldsymbol{x}}_j = \boldsymbol{F}_j(\boldsymbol{x}, \boldsymbol{u}_j), \quad \forall j = 1, \dots, N_{sys} \tag{2a}$$

$$\boldsymbol{y}_j = \boldsymbol{h}_j(\boldsymbol{x}_j, \boldsymbol{u}_j), \quad \forall j = 1, \dots, N_{sys} \tag{2b}$$

where N_{sys} denotes the number of subsystems, $\boldsymbol{x}_j \in \mathbb{R}^{n_j}$ and $\boldsymbol{u}_j \in \mathbb{R}^{m_j}$ are the state vector and control inputs for subsystem j, respectively. The overall system state vector is $\boldsymbol{x} = [\boldsymbol{x}_1^\top \dots \boldsymbol{x}_{N_{sys}}^\top]^\top \in \mathbb{R}^n$, where $n = \sum_{j=1}^{N_{sys}} n_j$, and the control input vector for the entire system is $\boldsymbol{u} = [\boldsymbol{u}_1^\top \dots \boldsymbol{u}_{N_{sys}}^\top]^\top \in \mathbb{R}^m$, where $m = \sum_{j=1}^{N_{sys}} m_j$. The control input for each subsystem j is constrained by $\boldsymbol{u}_j \in U_j := \{\boldsymbol{u}_{\mathbf{min},j_i} \le \boldsymbol{u}_{j_i} \le \boldsymbol{u}_{\mathbf{max},j_i}, \forall i = 1, 2, \cdots, m_j\} \in \mathbb{R}^{m_j}$, where $j = 1, \dots, N_{sys}$. The set U constraining the control input vector for the entire system is the union of the individual sets U_j, for all $j = 1, \dots, N_{sys}$.

2.3. Model predictive control

Model predictive control determines an optimal sequence of control inputs over a prediction horizon to minimize a cost function while satisfying system constraints. The MPC optimization problem is defined as:

$$\mathcal{J} = \min_{\boldsymbol{u}} \int_{t_k}^{t_{k+N_h}} L(\hat{\boldsymbol{y}}(t), \boldsymbol{u}(t))\, \mathrm{d}t \tag{3a}$$

$$\text{s.t. } \dot{\hat{\boldsymbol{x}}}(t) = \hat{\boldsymbol{F}}\left(\hat{\boldsymbol{x}}(t), \boldsymbol{u}(t)\right), \quad \hat{\boldsymbol{x}}(t_k) = \boldsymbol{x}(t_k) \tag{3b}$$

$$\hat{\boldsymbol{y}}(t) = \boldsymbol{h}(\hat{\boldsymbol{x}}(t), \boldsymbol{u}(t)) \tag{3c}$$

$$L(\hat{\boldsymbol{y}}(t), \boldsymbol{u}(t)) = (\hat{\boldsymbol{y}}(t) - \boldsymbol{y}_{sp})^\top \boldsymbol{A}(\hat{\boldsymbol{y}}(t) - \boldsymbol{y}_{sp}) + (\boldsymbol{u}(t) - \boldsymbol{u}_{sp})^\top \boldsymbol{B}(\boldsymbol{u}(t) - \boldsymbol{u}_{sp}) \tag{3d}$$

$$t \in [t_k, t_{k+N_h}) \tag{3e}$$

$$\|\boldsymbol{u}(t_k) - \boldsymbol{u}(t_{k-1})\| \le \Delta \boldsymbol{u}_{\text{limit}} \tag{3f}$$

$$\boldsymbol{u}(t) \in U \quad \forall t \in [t_k, t_{k+N_h}) \tag{3g}$$

where the objective function ($\mathcal{J}$) minimizes the deviation of the predicted output $\hat{\boldsymbol{y}}(t)$ from the setpoint $\boldsymbol{y}_{sp}$ and the control input $\boldsymbol{u}(t)$ from the reference $\boldsymbol{u}_{sp}$, weighted by matrices $\boldsymbol{A} = \left[A_{pq}\right]$ and $\boldsymbol{B} = \left[B_{pq}\right]$, which are diagonal, i.e., $A_{pq} = 0$ and $B_{pq} = 0$ for $p \neq q$. The state vector $\hat{\boldsymbol{x}}(t)$ is estimated by the designed (to be specified below) model $\hat{\boldsymbol{F}}\left(\hat{\boldsymbol{x}}(t), \boldsymbol{u}(t)\right)$. The constraints enforce control input rate limits ($\Delta \boldsymbol{u}_{\text{limit}}$) and ensure control inputs remain within the feasible set U.

2.4. Decentralized model predictive control

The optimization problem described in Section 2.3 incorporates all state variables and control inputs, a structure known as centralized MPC (CMPC). While CMPC is effective, it can become computationally expensive for large-scale or complicated systems. Decentralized model predictive control addresses this challenge by dividing the global optimization into smaller, localized problems, each handled by an individual MPC controller for the respective subsystem $j = 1, \dots, N_{sys}$.

Each local MPC controller for jth subsystem solves:

$$\mathcal{J}_j = \min_{\boldsymbol{u}_j} \int_{t_k}^{t_{k+N_h}} L_j(\hat{\boldsymbol{y}}_j(t), \boldsymbol{u}_j(t))\, \mathrm{d}t \tag{4a}$$

$$\text{s.t. } \dot{\hat{\boldsymbol{x}}}_j(t) = \hat{\boldsymbol{F}}_j\left(\hat{\boldsymbol{x}}_j(t), \boldsymbol{u}_j(t)\right), \quad \hat{\boldsymbol{x}}_j(t_k) = \boldsymbol{x}_j(t_k) \tag{4b}$$

$$\hat{\boldsymbol{y}}_j(t) = \boldsymbol{h}_j(\hat{\boldsymbol{x}}_j(t), \boldsymbol{u}_j(t)) \tag{4c}$$

$$L_j(\hat{\boldsymbol{y}}_j(t), \boldsymbol{u}_j(t)) = (\hat{\boldsymbol{y}}_j(t) - \boldsymbol{y}_{j,sp})^\top \boldsymbol{A}_j(\hat{\boldsymbol{y}}_j(t) - \boldsymbol{y}_{j,sp}) + (\boldsymbol{u}_j(t) - \boldsymbol{u}_{j,sp})^\top \boldsymbol{B}_j(\boldsymbol{u}_j(t) - \boldsymbol{u}_{j,sp}) \tag{4d}$$

$$t \in [t_k, t_{k+N_h}) \tag{4e}$$

$$\|\boldsymbol{u}_j(t_k) - \boldsymbol{u}_j(t_{k-1})\| \leq \Delta \boldsymbol{u}_{\text{limit},j} \tag{4f}$$

$$\boldsymbol{u}_j(t) \in U_j \quad \forall t \in [t_k, t_{k+N_h}) \tag{4g}$$

where the objective function ($\mathcal{J}_j$) minimizes the deviation of the predicted output $\hat{\boldsymbol{y}}_j(t)$ from the setpoint $\boldsymbol{y}_{j,sp}$ and the control input $\boldsymbol{u}_j(t)$ from the reference $\boldsymbol{u}_{j,sp}$, weighted by matrices $\boldsymbol{A} = \left[A_{j,pq}\right]$ and $\boldsymbol{B} = \left[B_{j,pq}\right]$, which are diagonal, i.e., $A_{j,pq} = 0$ and $B_{j,pq} = 0$ for $p \neq q$. The state vector $\hat{\boldsymbol{x}}_j(t)$ is estimated by the designed model $\hat{\boldsymbol{F}}_j\left(\hat{\boldsymbol{x}}_j(t), \boldsymbol{u}_j(t)\right)$. The constraints enforce control input rate limits ($\Delta \boldsymbol{u}_{\text{limit},j}$) and ensure control inputs remain within the feasible set U_j.

2.5. Disturbance observer

For this specific work, the disturbance observer formulation is developed from the offset-free method, which is also one type of the extended state observer. This allows the system to correct errors by introducing an additional disturbance state (extended state), $\boldsymbol{\xi} \in \mathbb{R}^m$. Additionally, the state observer is also designed to estimate the state. The offset-free approach can be represented by the following set of equations (Maeder et al., 2009; Wang et al., 2024; Wallace et al., 2016):

$$\dot{\tilde{\boldsymbol{x}}} = \hat{\boldsymbol{F}}(\tilde{\boldsymbol{x}}, \boldsymbol{u}) + \boldsymbol{L}_{\boldsymbol{x}}(\boldsymbol{y} - \tilde{\boldsymbol{y}}) + \boldsymbol{B}_{\boldsymbol{d}}\boldsymbol{\xi} \tag{5a}$$

$$\tilde{\boldsymbol{y}} = \boldsymbol{h}(\tilde{\boldsymbol{x}}, \boldsymbol{u}) \tag{5b}$$

$$\dot{\boldsymbol{\xi}} = \boldsymbol{L}_{\boldsymbol{\xi}}(\boldsymbol{y} - \tilde{\boldsymbol{y}}) \tag{5c}$$

where $\tilde{\boldsymbol{x}} \in \mathbb{R}^n$ is the modified state vector governed by the system dynamics with augmented state observer and disturbance accumulation. $\boldsymbol{L}_{\boldsymbol{x}} \in \mathbb{R}^{n\times k}$ and $\boldsymbol{L}_{\boldsymbol{\xi}} \in \mathbb{R}^{n\times k}$ serves as the observer gains, and $(\boldsymbol{y} - \tilde{\boldsymbol{y}}) \in \mathbb{R}^k$ is the error between the real output $\boldsymbol{y} \in \mathbb{R}^k$ and the expected output $\tilde{\boldsymbol{y}} \in \mathbb{R}^k$. The additional disturbance state $\boldsymbol{\xi} \in \mathbb{R}^n$ corrects for model inaccuracies by accumulating the error. $\boldsymbol{B}_{\boldsymbol{d}} \in \mathbb{R}^{n\times n}$ represents the disturbance matrix.

Building on the offset-free method, the unknown input observer (UIO), which is a type of disturbance observer that explicitly estimates disturbances and integrates them into the system model (Chen et al., 2015). In this technique, the disturbances are assumed to be generated by the following exogenous system (Johnson, 1970; Chen et al., 1996):

$$\dot{\boldsymbol{\xi}} = \boldsymbol{W}\boldsymbol{\xi} \tag{6a}$$

$$\boldsymbol{d} = \boldsymbol{V}\boldsymbol{\xi} \tag{6b}$$

where $\boldsymbol{W} \in \mathbb{R}^{n\times n}$ and $\boldsymbol{V} \in \mathbb{R}^{n\times n}$ are designed diagonal matrices. Specifically, the disturbance term is introduced to capture the mismatch between the actual process dynamics and the model used in the MPC. Therefore, the DOB equations are formulated by introducing a new disturbance term $\tilde{\boldsymbol{d}} \in \mathbb{R}^n$ that is computed from the auxiliary state $\tilde{\boldsymbol{\xi}} \in \mathbb{R}^n$ to Eq. (5), as shown in the following equation:

$$\dot{\tilde{\boldsymbol{x}}} = \hat{\boldsymbol{F}}(\tilde{\boldsymbol{x}}, \boldsymbol{u}) + \boldsymbol{L}_{\boldsymbol{x}}(\boldsymbol{y} - \tilde{\boldsymbol{y}}) + \boldsymbol{B}_{\boldsymbol{d}}\tilde{\boldsymbol{d}} \tag{7a}$$

$$\tilde{\boldsymbol{y}} = \boldsymbol{h}(\tilde{\boldsymbol{x}}) \tag{7b}$$

$$\dot{\tilde{\boldsymbol{\xi}}} = \boldsymbol{W}\tilde{\boldsymbol{\xi}} + \boldsymbol{L}_{\boldsymbol{\xi}}(\boldsymbol{y} - \tilde{\boldsymbol{y}}) \tag{7c}$$

$$\tilde{\boldsymbol{d}} = \boldsymbol{V}\tilde{\boldsymbol{\xi}} \tag{7d}$$

where $\tilde{\boldsymbol{d}} \in \mathbb{R}^n$ estimates the disturbance $\boldsymbol{d} \in \mathbb{R}^n$ in Eq. (6) calculated using $\boldsymbol{V}\tilde{\boldsymbol{\xi}} \in \mathbb{R}^n$. Based on Eq. (7), the model utilized in MPC is formulated by combining the state variables and the observer variables as follows:

$$\dot{\bar{\boldsymbol{x}}} = \bar{\boldsymbol{F}}(\bar{\boldsymbol{x}}, \boldsymbol{u}) \tag{8a}$$

$$\bar{\boldsymbol{y}} = \boldsymbol{h}(\bar{\boldsymbol{x}}) \tag{8b}$$

$$\bar{\boldsymbol{x}} = \begin{bmatrix}\tilde{\boldsymbol{x}} \\ \tilde{\boldsymbol{\xi}}\end{bmatrix}, \quad \bar{\boldsymbol{F}}(\bar{\boldsymbol{x}}, \boldsymbol{u}) = \begin{bmatrix}\hat{\boldsymbol{F}}(\tilde{\boldsymbol{x}}, \boldsymbol{u}) + \boldsymbol{B}_{\boldsymbol{d}}\tilde{\boldsymbol{d}} \\ \boldsymbol{W}\tilde{\boldsymbol{\xi}}\end{bmatrix} \tag{8c}$$

For the subsystem j, this augmented model is as follows:

$$\dot{\bar{\boldsymbol{x}}}_j = \bar{\boldsymbol{F}}_j(\bar{\boldsymbol{x}}_j, \boldsymbol{u}_j) \tag{9a}$$

$$\bar{\boldsymbol{y}}_j = \boldsymbol{h}_j(\bar{\boldsymbol{x}}_j) \tag{9b}$$

$$\bar{\boldsymbol{x}}_j = \begin{bmatrix}\tilde{\boldsymbol{x}}_j \\ \tilde{\boldsymbol{\xi}}_j\end{bmatrix}, \quad \bar{\boldsymbol{F}}_j(\bar{\boldsymbol{x}}_j, \boldsymbol{u}_j) = \begin{bmatrix}\hat{\boldsymbol{F}}_j(\tilde{\boldsymbol{x}}_j, \boldsymbol{u}_j) + \boldsymbol{B}_{\boldsymbol{d},j}\tilde{\boldsymbol{d}}_j \\ \boldsymbol{W}_j\tilde{\boldsymbol{\xi}}_j\end{bmatrix} \tag{9c}$$

Since the model is corrected over time, the reference control input vector setpoints ($\boldsymbol{u}_{sp}$) must also be changed. To estimate $\boldsymbol{u}_{sp}$, the condition in which state variables are at a steady state and the control target has reached the controlled setpoints is assumed. Therefore,

$$\bar{\boldsymbol{F}}(\bar{\boldsymbol{x}}_{sp}, \boldsymbol{u}_{sp}) = \boldsymbol{0}, \tag{10a}$$

$$\boldsymbol{h}(\bar{\boldsymbol{x}}_{sp}, \boldsymbol{u}_{sp}) = \boldsymbol{y}_{sp}. \tag{10b}$$

The solution ($\bar{\boldsymbol{x}}^*_{sp}, \boldsymbol{u}^*_{sp}$) of Eq. (10) is the corresponding state vector and reference control input vector at the setpoints. However, if multiple solutions or no solution exists within the feasible region for Eq. (10), these equations cannot be effectively employed to determine $\boldsymbol{u}_{sp}$. Therefore, to ensure the uniqueness of the solution for Eq. (10) within the feasible regions, the following conditions must be satisfied.

Firstly, the number of equations should be matched to the number of unknowns. Therefore,

$$\dim(\bar{\boldsymbol{F}}) + \dim(\boldsymbol{h}) = n + m, \tag{11}$$

where $n = \dim(\bar{\boldsymbol{x}}_{sp})$ and $m = \dim(\boldsymbol{u}_{sp})$. From the definition, $m = k$ is needed to satisfy this condition. This condition guarantees the possibility of a unique solution. Additionally, the functions $\bar{\boldsymbol{F}}$ and $\boldsymbol{h}$ are supposed to be continuously differentiable. Formally, this means:

$$\bar{\boldsymbol{F}} \in C^1(\mathbb{R}^{n+m}, \mathbb{R}^n), \quad \boldsymbol{h} \in C^1(\mathbb{R}^{n+m}, \mathbb{R}^m) \tag{12}$$

which is used to prove continuous differentiability and ensures that the system is smooth enough to apply differential methods like the Implicit Function Theorem or Newton–Raphson methods to calculate the steady states.

The Jacobian matrix $\boldsymbol{J}$ of the system with respect to the variables $(\bar{\boldsymbol{x}}_{sp}, \boldsymbol{u}_{sp})$ is also considered. The Jacobian is given by:

$$\boldsymbol{J} = \begin{bmatrix} \dfrac{\partial \bar{\boldsymbol{F}}}{\partial \bar{\boldsymbol{x}}_{sp}} & \dfrac{\partial \bar{\boldsymbol{F}}}{\partial \boldsymbol{u}_{sp}} \\ \dfrac{\partial \boldsymbol{h}}{\partial \bar{\boldsymbol{x}}_{sp}} & \dfrac{\partial \boldsymbol{h}}{\partial \boldsymbol{u}_{sp}} \end{bmatrix}. \tag{13}$$

This Jacobian matrix must be nonsingular at the solution point $(\bar{\boldsymbol{x}}^*_{sp}, \boldsymbol{u}^*_{sp})$, which is mathematically expressed as:

$$\det(\boldsymbol{J}) \neq 0. \tag{14}$$

This condition guarantees the local uniqueness of the solution and ensures that the system behaves well under small perturbations.

Finally, the global uniqueness of the solution $(\bar{\boldsymbol{x}}^*_{sp}, \boldsymbol{u}^*_{sp})$ is established by reformulating the system as a contraction mapping and applying the Banach Fixed-Point Theorem (Khamsi and Kirk, 2011). The vector $\boldsymbol{z}$ and the mapping $\boldsymbol{T}$ are defined as follows:

$$\boldsymbol{z} = \begin{bmatrix} \bar{\boldsymbol{x}}_{sp} \\ \boldsymbol{u}_{sp} \end{bmatrix}, \quad \boldsymbol{T}(\boldsymbol{z}) = \begin{bmatrix} \boldsymbol{T}_{\bar{x}}(\boldsymbol{z}) \\ \boldsymbol{T}_{u}(\boldsymbol{z}) \end{bmatrix}, \tag{15}$$

where $\boldsymbol{T}_{\bar{x}}$ and $\boldsymbol{T}_u$ are defined based on the original Eq. (10), as follows:

$$\boldsymbol{T}_{\bar{x}}(\boldsymbol{z}) = \bar{\boldsymbol{x}}_{sp} - \alpha\, \bar{\boldsymbol{F}}(\bar{\boldsymbol{x}}_{sp}, \boldsymbol{u}_{sp}), \tag{16}$$

$$\boldsymbol{T}_{u}(\boldsymbol{z}) = \boldsymbol{u}_{sp} - \beta \left(\boldsymbol{h}(\bar{\boldsymbol{x}}_{sp}, \boldsymbol{u}_{sp}) - \boldsymbol{y}_{sp} \right), \tag{17}$$

where α and β are appropriately chosen constants.

The Lipschitz condition with Lipschitz constant $L < 1$ must also be satisfied for the designed function $\boldsymbol{T}$:

$$\|\boldsymbol{T}(\boldsymbol{z}_1) - \boldsymbol{T}(\boldsymbol{z}_2)\| \leq L \cdot \|\boldsymbol{z}_1 - \boldsymbol{z}_2\|, \tag{18}$$

for all $\boldsymbol{z}_1, \boldsymbol{z}_2 \in \mathbb{R}^{n+m}$. This can be achieved by bounding the norms of the differences:

$$\|\boldsymbol{T}_{\bar{x}}(\boldsymbol{z}_1) - \boldsymbol{T}_{\bar{x}}(\boldsymbol{z}_2)\| \leq \alpha\, L_{\bar{F}} \|\boldsymbol{z}_1 - \boldsymbol{z}_2\|, \tag{19}$$

$$\|\boldsymbol{T}_{u}(\boldsymbol{z}_1) - \boldsymbol{T}_{u}(\boldsymbol{z}_2)\| \leq \beta\, L_{h} \|\boldsymbol{z}_1 - \boldsymbol{z}_2\|, \tag{20}$$

where $L_{\bar{F}}$ and L_h are Lipschitz constants for $\bar{\boldsymbol{F}}$ and $\boldsymbol{h}$, respectively. α and β are chosen to ensure that $\boldsymbol{T}$ is a contraction:

$$\alpha L_{\bar{F}} + \beta L_h < 1. \tag{21}$$

Since $\mathbb{R}^{n+m}$ equipped with the standard Euclidean norm is a complete metric space, by the Banach Fixed-Point Theorem, the mapping $\boldsymbol{T}$ has a unique fixed point in $\mathbb{R}^{n+m}$. This uniqueness is established by the contraction property, which ensures that the function, when iterated from any initial point, converges towards the fixed point. This fixed point corresponds to the unique solution $(\bar{\boldsymbol{x}}^*_{sp}, \boldsymbol{u}^*_{sp})$ of Eq. (10).

Under the conditions of dimensional consistency Eq. (11), continuous differentiability Eq. (12), nonsingularity of the Jacobian Eq. (14), and the contraction mapping condition Eq. (21), both local and global uniqueness of the steady state solutions $(\bar{\boldsymbol{x}}^*_{sp}, \boldsymbol{u}^*_{sp})$ within the feasible region are established. This ensures that the unique set of reference control input setpoints can be adaptively changed. If the solution of Eq. (10) is not unique, $\boldsymbol{B}$ or $\boldsymbol{B}_j$ are required to be set as $\boldsymbol{0}$ in Eqs. (3d) and (4d), respectively.

Remark 1. In particular, if $\boldsymbol{W} = 0$ and $\boldsymbol{V} = I$, it is equivalent to Eq. (5). Thus, $\boldsymbol{W} = 0$ and $\boldsymbol{V} = I$ are set as the initial values when tuning the disturbance observer. Finally, both parameters are carefully tuned to optimize performance.

2.6. Protonic membrane reformer

The PMR process generates hydrogen along with carbon monoxide (CO) and carbon dioxide (CO_2) as byproducts (Eq. (22)).

$$CH_4 + H_2O \rightleftharpoons 3H_2 + CO, \ \Delta H_{298} = 206.1 \text{ kJ mol}^{-1} \tag{22a}$$

$$CO + H_2O \rightleftharpoons CO_2 + H_2, \ \Delta H_{298} = -41.15 \text{ kJ mol}^{-1} \tag{22b}$$

A PMR unit simultaneously permeates protons from its anodic gas mixture through a solid oxide electrolyte to purify the H_2 target product. The driving force for H_2 separation from the ionized H^+ atoms in the anode to the cathode is the potential gradient produced by a power supply. An electrochemical surface reaction allows for the recombination of H^+ with electrons to reform H_2 gas in the high-pressure cathode of the PMR.

$$H_2 \rightleftharpoons 2H^+ + 2e^- \tag{23}$$

This integrated system offers a more efficient pathway for hydrogen production by combining reforming, purification, and compression processes within a single unit. In contrast, a conventional SMR plant necessitates multiple discrete units to achieve the same outcomes (Molburg and Doctor, 2003; Taji et al., 2018; Hsu et al., 2024).

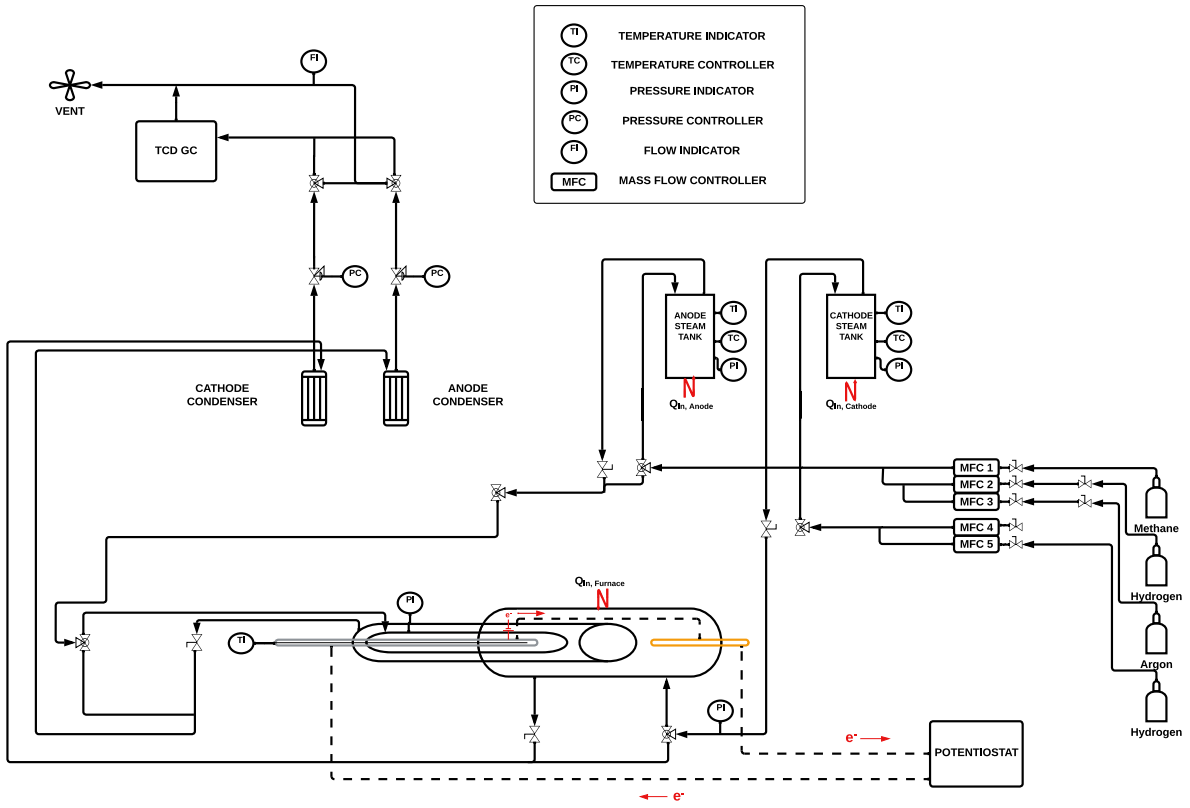

Fig. 1. Overall piping and instrumentation schematic to demonstrate the location of the PMR system process units, sensors, and actuators.

2.7. Experimental methods

2.7.1. PMR system

The PMR system at UCLA was built to convert methane and steam into carbon monoxide, carbon dioxide, and hydrogen. Fig. 1 displays a P&ID diagram showing the PMR process gas flow, piping, sensors, and actuators. Argon (Ar) is used as a gas chromatogram (GC) tracer during experiments to account for volumetric flowrate changes in the gas product mixture caused by the overall stoichiometry of the gas-phase SMR reactions. Along with argon, hydrogen is fed to the reactor unit to prevent unwanted side reactions that produce solid carbon and to simulate the existence of a pre-reformer. All reactants flow through the anode, or the retentate region, of the reactor. At the same time, a mixture of steam and hydrogen flow as carrier gases through the cathode, or permeate region, of the PMR where electrochemically separated hydrogen is collected. The system is configured such that a carrier gas is needed to move steam from the steam-generating bubblers to the permeate side of the proton membrane reformer unit. Hydrogen is used as a carrier because the downstream digital flow meter, located after the steam-removing condensers, can only accurately measure a pure gas species flowrate. Thus, if hydrogen is the carrier gas in the cathode that is mixed with the hydrogen that flows to the permeate side of the membrane through electrochemical separation, a pure species flows through the digital flow meter that is used to track the hydrogen volumetric flowrate.

The experimental system pressure is 1 bar at the anode and 1 bar at the cathode. During operation, the inlet gases travel through two bubblers that wet the gas mixtures in the anode and cathode. A steam-to-carbon ratio of 3 is used in the anode gas mixture, while a 67% steam mixture flows through the cathode side of the reformer. Next, the reactant gases flow into the anode of the PMR where Ni catalytic sites are embedded into the surface of the anodic electrode. The SMR and WGS reactions take place at the anodic electrode, and concurrently, dihydrogen gas splits into protons that are separated through the solid electrolyte housed between the electrodes. Once the protons travel through the electrolyte and through the cathodic electrode, the individual hydrogen atoms meet with available electrons and reform dihydrogen gas, demonstrating a primary driving force for separation that is a function of the potential difference between the anode and cathode of the membrane. Unreacted gases and unremoved species remain in the anode and exit the reactor to be quantified in a TCD GC after excess steam is removed with a condenser. The removed hydrogen species exit the reactor cathode, and the flowrate of the separated hydrogen is measured downstream after cathodic steam is also removed with a condenser.

2.7.2. Actuators and sensors

The experimental PMR system is equipped with temperature indicators and actuators, pressure indicators and actuators, flow indicators and actuators, a potentiostat, and a TCD GC. All sensors and actuators are recorded on a per second basis into a LabVIEW user interface with a CompactRIO analog-to-digital signal converter. The four mass flow controllers measure and modulate all inlet gas flowrates. A flowmeter measures the total hydrogen flowrate in the cathode before the molecular hydrogen gas exits the system through a vent. Four pressure indicators transmit the pressures in the anode and cathode steam tanks, the cathode reactor inlet, and the anode reactor outlet. Back pressure regulators, or pressure controllers, set the pressures on either side of the PMR system. Two temperature controllers are located in the steam bubblers to control the vapor pressure of steam, and three temperature indicators are located in the two steam tanks and the anode inlet of the PMR. Finally, a potentiostat is

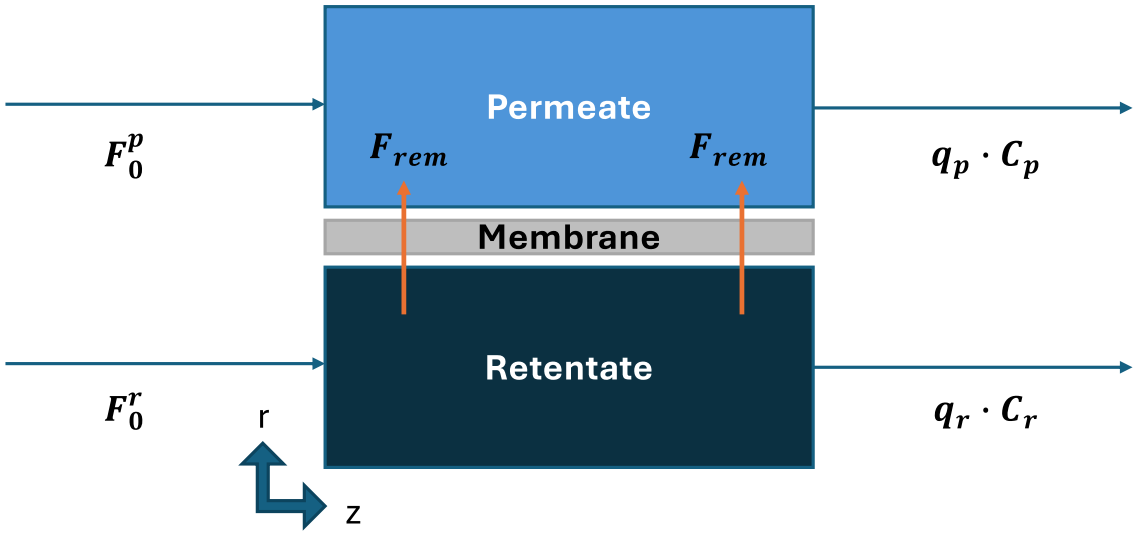

Fig. 2. Schematic describing the molar flow of retentate and permeate inlet species through the CST-MR control volume, through a generic proton conducting membrane, and to the retentate and permeate outlets of the reactor.

used to measure and control the potential across the closed circuit of the PMR, along with an automated GC that measures the composition of the anode species after leaving the PMR.

Remark 2. Each gas species flowrate from the reactor is measured using GC and expressed in standard cubic centimeters per minute (sccm). Due to the GC cooling period and analysis time, sampling is performed at 18-min intervals with a 15-min delay, resulting in infrequent and delayed gas measurement data. In contrast, the temperature indicators and digital flowmeter provide data in real time on a per second basis.

3. Model development and validation

In this section, a first principles model of the entire PMR system is derived from a classic reaction engineering CSTR model in order to capture the dynamic behavior of a general gas-phase CST-MR. Subsequently, this model is applied to the PMR system, and a model for a gas bubbler is developed to estimate the steam flowrate in the reactor inlet gas mixture. A CST-MR operates like a typical CSTR but incorporates a membrane within the reactor. This membrane allows for selective separation or removal of selected components during the reaction. In a CST-MR, the side of the membrane with unremoved gas species is referred to as the retentate, and the side of the membrane through which the removed species travel is called the permeate (Barbieri, 2015). The schematic of a general CST-MR is illustrated in Fig. 2.

3.1. Gas-phase CST-MR dynamic model

To develop the dynamic model of a CST-MR process, a traditional CSTR model is adapted. For a dynamic CSTR model, the mole balance of each gas species is presented as follows:

$$F_{i,0} + R_{i,gen} = qC_i + V\dot{C}_i \tag{24}$$

where i refers to all species in the reactor. In general, this equation reveals that the incoming species must exit the reactor outlet or accumulate within the reactor control volume. Based on this, the mole balance for a gas-phase CST-MR retentate is developed. For the retentate side of a CST-MR, the mole balance is as follows:

$$F^r_{j,0} + R_{j,gen} = q^r C^r_j + V^r \dot{C}^r_j \tag{25a}$$

$$F^r_{k,0} + R_{k,gen} = q^r C^r_k + F_{k,rem} + V^r \dot{C}^r_k \tag{25b}$$

Where j and k refer to each unremoved or removed species, respectively. Based on rearranging of Eq. (25), a dynamic model for the retentate is developed:

$$\dot{\boldsymbol{C}}^{\boldsymbol{r}} = \frac{1}{V^r}\left(\boldsymbol{F}^{\boldsymbol{r}}_{\boldsymbol{0}} + \boldsymbol{R}_{\boldsymbol{gen}} - q^r\,\boldsymbol{C}^{\boldsymbol{r}} - \boldsymbol{F}_{rem}\right) \tag{26a}$$

$$\boldsymbol{C}^{\boldsymbol{r}} = \begin{bmatrix} C^r_j \\ C^r_k \end{bmatrix}, \quad \boldsymbol{F}^{\boldsymbol{r}}_{\boldsymbol{0}} = \begin{bmatrix} F^r_{j,0} \\ F^r_{k,0} \end{bmatrix}, \quad \boldsymbol{R}_{\boldsymbol{gen}} = \begin{bmatrix} R_{j,gen} \\ R_{k,gen} \end{bmatrix}, \quad \boldsymbol{F}_{rem} = \begin{bmatrix} 0 \\ F_{k,rem} \end{bmatrix} \tag{26b}$$

where the dynamic behavior of the species concentration in the retentate is described by this ordinary differential equation (ODE). However, due to gas-phase thermodynamic properties, the volumetric flowrate (q^r in Eq. (26)) in the retentate changes with the progression of SMR reactions and hydrogen extraction. To determine q^r, the ideal gas law is involved as shown in Eq. (27).

$$\sum C^r_i = \frac{P^r}{RT^r} \tag{27}$$

Where $i = j + k$ refers to each species in the retentate. From the ideal gas law, and with the assumption of constant pressure, the sum of the derivative of each species concentration can be expressed as Eq. (28).

$$\sum \dot{C}_i^r = -\frac{P^r}{R(T^r)^2}\dot{T}^r \tag{28}$$

From Eq. (26), the sum of the derivative of each species concentration can also be presented as:

$$\sum \dot{C}_i^r = \frac{1}{V^r}\left(\sum F_{i,0}^r + \sum R_{j,gen} + \sum R_{k,gen} - q^r \sum C_i^r - \sum F_{k,rem}\right) \tag{29}$$

By combining Eqs. (27), (28) and (29), the volumetric flowrate is calculated by Eq. (30).

$$q^r = \left(\sum F_{i,0}^r + \sum R_{j,gen} + \sum R_{k,gen} - \sum F_{k,rem}\right)\frac{RT^r}{P^r} + \frac{V^r}{T^r}\dot{T}^r \tag{30}$$

In the CST-MR dynamic model, an energy balance is formulated to monitor the transient reactor temperature, which can also be regarded as a state variable. For a conventional CSTR, the energy balance is generally expressed as Eq. (31) (Abdalah, 2020), under the assumptions of negligible heat generation from the stirrer.

$$\dot{T} = \frac{\dot{Q}_h + \dot{Q}_s + \dot{Q}_r + \dot{Q}_l}{\sum \rho_i C_{p,i} V} \tag{31a}$$

$$\dot{Q}_s = \sum F_{i,0}\int_{T_0}^{T} C_{p,i}dT' \tag{31b}$$

$$\dot{Q}_r = -\sum R_j \Delta H_j(T) \tag{31c}$$

$$\dot{Q}_l = U_h A_h (T^a - T) \tag{31d}$$

Where $\dot{Q}_h$, $\dot{Q}_s$, $\dot{Q}_r$ and $\dot{Q}_l$ refer to the energy associated with the heat source, enthalpy of inlet gas streams, the endothermic and/or exothermic reactions, and heat loss to the surroundings, respectively.

For the CST-MR, the temperature of the retentate is also influenced by the species extraction process, particularly when the driving force for separation is an electric potential gradient across the membrane. Heat transfer via conduction occurs through the membrane material as well. Considering these phenomena, the retentate energy balance is written as follows:

$$\dot{T}^r = \frac{\dot{Q}_h^r + \dot{Q}_s^r + \dot{Q}_r^r + \dot{Q}_l^r + \dot{Q}_e^r + \dot{Q}_p^r}{\sum \rho_i^r C_{p,i} V^r} \tag{32a}$$

$$\dot{Q}_s^r = \sum F_{i,0}^r \int_{T_0^r}^{T^r} C_{p,i}dT' \tag{32b}$$

$$\dot{Q}_r^r = -\sum R_j \Delta H_j(T^r) \tag{32c}$$

$$\dot{Q}_l^r = U_h^r A_h^r (T^a - T^r) \tag{32d}$$

Where $\dot{Q}_h^r$, $\dot{Q}_s^r$, $\dot{Q}_r^r$ and $\dot{Q}_l^r$ refer to the heat transfer rate associated with the heat source, enthalpy of inlet gas stream, the endothermic and/or exothermic reactions and the heat loss to the surroundings, respectively, for the retentate of a CST-MR process. Additional terms $\dot{Q}_e^r$ and $\dot{Q}_p^r$ are considered in the CST-MR energy balance, referring to the energy caused by the species extraction process and heat transfer from the permeate to quantify heat generation at the membrane interface.

For the permeate, the membrane-extracted gas species are inputs to the material balance. Thus, the mole balance for permeate species follows:

$$F_{m,0}^p = q^p C_m^p + V^p \dot{C}_m^p \tag{33a}$$

$$F_{k,0}^p + F_{k,rem} = q^p C_k^p + V^p \dot{C}_k^p \tag{33b}$$

In this formulation, m represents the carrier gas species in the permeate. By rearranging Eq. (33), the dynamic model for the concentration of each permeate species can be expressed as:

$$\dot{\boldsymbol{C}}^{\boldsymbol{p}} = \frac{1}{V^p}\left(\boldsymbol{F}_{\boldsymbol{0}}^{\boldsymbol{p}} - q^p \boldsymbol{C}^{\boldsymbol{p}} + \boldsymbol{F}_{rem}\right) \tag{34a}$$

$$\boldsymbol{C}^{\boldsymbol{p}} = \begin{bmatrix} C_m^p \\ C_k^p \end{bmatrix}, \quad \boldsymbol{F}_{\boldsymbol{0}}^{\boldsymbol{p}} = \begin{bmatrix} F_{m,0}^p \\ F_{k,0}^p \end{bmatrix}, \quad \boldsymbol{F}_{rem} = \begin{bmatrix} 0 \\ F_{k,rem} \end{bmatrix} \tag{34b}$$

Similar to the case for the retentate, upon applying the ideal gas law to the permeate gas species concentrations, the derivative of the total gas concentration in the permeate can be expressed as:

$$\sum \dot{C}_i^p = -\frac{P^p}{R(T^p)^2}\dot{T}^p \tag{35a}$$

$$\sum \dot{C}_i^p = \frac{1}{V^p}\left(\sum F_{i,0}^p - q^p \sum C_i^p + \sum F_{k,rem}\right) \tag{35b}$$

Therefore, combining Eqs. (35a) and (35b), the total volumetric flowrate in the permeate is calculated by:

$$q^p = \left(\sum F_{l,0}^p + \sum F_{k,rem}\right)\frac{RT^p}{P^p} + \frac{V^p}{T^p}\dot{T}^p \tag{36}$$

where $l = m + k$ is denoted as all gases in the permeate and T^p is determined by the energy balance of the permeate, shown as follows:

$$\dot{T}^p = \frac{\dot{Q}_h^p + \dot{Q}_s^p + \dot{Q}_l^p + \dot{Q}_e^p + \dot{Q}_r^p}{\sum \rho_i^p C_{p,i} V^p} \tag{37a}$$

$$\dot{Q}_s^p = \sum F_{i,0}^p \int_{T_0^p}^{T^p} C_{p,i}dT' + \sum F_{k,rem}\int_{T^r}^{T^p} C_{p,k}dT' \tag{37b}$$

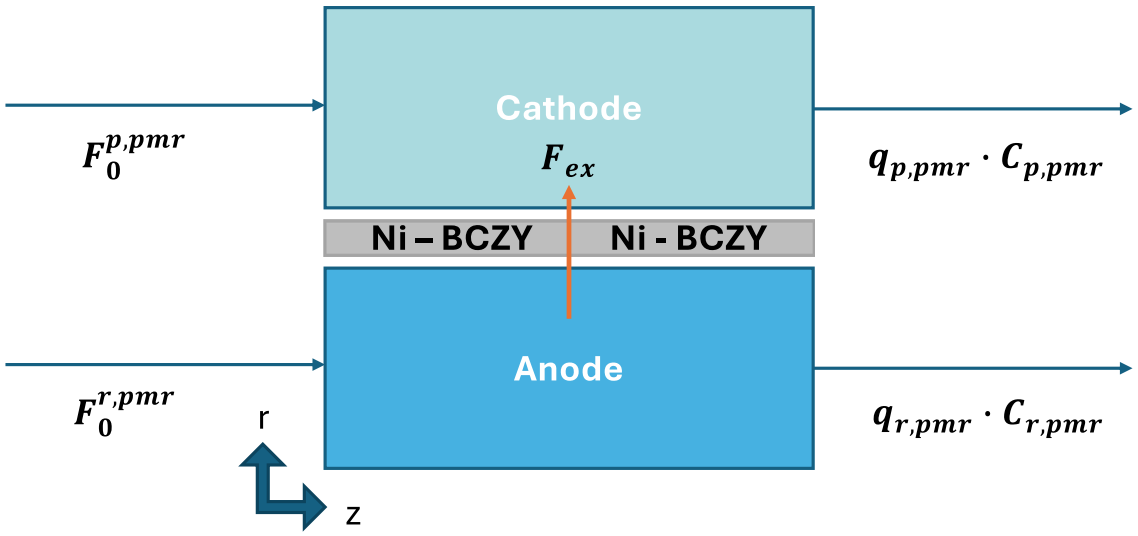

Fig. 3. Schematic describing the molar flow of anode (retentate) and cathode (permeate) inlet species through the PMR control volume, through the Ni-BCZY proton conducting membrane, and to the anode and cathode outlets.

$$\dot{Q}_l^p = U_h^p A_h^p (T^a - T^p) \tag{37c}$$

where $\dot{Q}_h^p$, $\dot{Q}_s^p$, $\dot{Q}_l^p$, $\dot{Q}_e^p$ and $\dot{Q}_r^p$ refer to the heat transfer rate associated with the heat source, enthalpy of inlet gas streams, the heat loss to the surroundings, resistive-heat due to species extraction, and heat transfer from the retentate region, respectively, for the permeate of a CST-MR process.

Therefore, the gas-phase CST-MR first principles model can be presented as follows:

$$\boldsymbol{x}_{\boldsymbol{CST-MR}} = \begin{bmatrix} C^r \\ T^r \\ C^p \\ T^p \end{bmatrix} \tag{38}$$

3.2. PMR model

The gas-phase CST-MR model developed in Section 3.1 is now applied to the PMR process illustrated in Fig. 3 based on the following considerations:

- Reaction characteristics: The reactions involved in the SMR process are slow relative to the time required for back mixing, resulting in near-complete conversion at the initial length of the reactor. Consequently, species concentrations and reactor temperatures remain relatively uniform throughout the reactor length (Cui et al., 2024).
- Phase characteristics: Since all reactants and products are in the gas phase, at a significantly high temperature, effective species mixing is achieved even without mechanical stirring.
- Computational efficiency: In comparison to other dynamic models, such as packed bed reactors (PBR), this lumped-parameter model is simpler, leading to reduced computational time. This efficiency makes it well-suited for real time implementation in an MPC scheme.

However, to implement the gas-phase CST-MR model, additional parameters, including the H_2 extraction rate, SMR reaction kinetics, and the electrochemical extraction energy, must be defined.

Since the extraction process is driven by a potential gradient, the H_2 extraction rate ($F_{H_2,ex}$ is determined based on the electron balance across the membrane (Wrubel et al., 2021), as presented in Eq. (39):

$$n_e F_a F_{H_2,ex} = \eta_F I_m \tag{39}$$

where the n_e represents the moles of electrons transferred per mole of removed species. According to Eq. (23), $n_e = 2$ mol-e/mol. F_a is the Faraday's constant, representing the magnitude of electric charge per mole of electrons. η_F is the Faradaic efficiency. In this case, a 100% Faradaic efficiency is assumed. After rearranging Eq. (39), the H_2 extraction rate can be expressed as Eq. (40).

$$F_{H_2,ex} = \frac{I_m}{2F_a} \tag{40}$$

For balances derived in Section 3.1, reaction kinetics must also be determined. Specifically, the rate expressions of the PMR process are modeled using the Langmuir-Hinshelwood-Hougen-Watson (LHHW) formalism, a widely adopted framework for heterogeneous catalytic reactions, and

Table 1
Gas species generation rate in the PMR control volume due to SMR and WGS chemical reactions.

Gas species	Generation rate
CH_4	$R_{CH_4} = -r_1 W_{cat}$
H_2O	$R_{H_2O} = (-r_1 - r_2) W_{cat}$
CO	$R_{CO} = r_1 W_{cat}$
H_2	$R_{H_2} = (3r_1 + r_2) W_{cat}$
CO_2	$R_{CO_2} = -r_2 W_{cat}$
Ar	$R_{Ar} = 0$

adopts the kinetic parameters put forth in Xu and Froment (1989), as presented below:

$$r_1 = \frac{k_1}{P_{H_2}^{2.5}} \frac{P_{CH_4} P_{H_2O} - \frac{P_{H_2}^3 P_{CO}}{K_1}}{(DEN)^2} \tag{41a}$$

$$r_2 = \frac{k_2}{P_{H_2}} \frac{P_{CO} P_{H_2O} - \frac{P_{H_2} P_{CO_2}}{K_2}}{(DEN)^2} \tag{41b}$$

$$DEN = 1 + K_{CO} P_{CO} + K_{H_2} P_{H_2} + K_{CH_4} P_{CH_4} + K_{H_2O} \frac{P_{H_2O}}{P_{H_2}} \tag{41c}$$

where r_1 and r_2 are kinetic rates for the SMR reaction (Eq. (22a)) and the WGS reaction (Eq. (22b)), respectively. In this equation, the partial pressure P_i for gas species i, where $i = CH_4, H_2O, CO, H_2, CO_2, Ar$, can be determined based on Dalton's law and the ideal gas law:

$$P_i = \frac{C_i}{RT} \tag{42}$$

To determine rate constants and adsorption coefficients, an Arrhenius-type expression is assumed:

$$k_j = A_j \exp\left(-\frac{E_j}{RT}\right), \quad j = 1, 2 \tag{43a}$$

$$K_i = A_i \exp\left(-\frac{\Delta H_i}{RT}\right), \quad i = CH_4, H_2O, CO, H_2 \tag{43b}$$

To further determine generation rates of all gas species, the stoichiometric ratios in the SMR and WGS reactions (Eq. (22)) are considered and summarized in Table 1.

By applying these defined parameters to the anode based on Eqs. (27), (30) and (40), the volumetric flowrate ($q^{a,PMR}$) can be expressed as follows:

$$q^{a,PMR} = \left(\sum F_{i,0}^{a,PMR} + 2r_1 W_{cat} - \frac{I_m}{2F_a}\right) \frac{RT^{a,PMR}}{P^{a,PMR}} + \frac{V^{a,PMR}}{T^{a,PMR}} \dot{T}^{a,PMR} \tag{44}$$

where $i = CH_4, H_2O, CO, H_2, Ar$. Additionally, based on Eqs. (26), (40), (41), (43), (44) and Table 1, the dynamic model for the concentrations of all gas species in the anode of the PMR is developed as follows:

$$\dot{\boldsymbol{C}}^{\boldsymbol{a,PMR}} = \frac{\boldsymbol{F_0^{a,PMR}} + \boldsymbol{R} - q^{a,PMR} \boldsymbol{C}^{\boldsymbol{a,PMR}} - \boldsymbol{F_{ex}}}{V^{a,PMR}} \tag{45a}$$

$$\boldsymbol{C}^{\boldsymbol{a,PMR}} = \begin{bmatrix} C_{CH_4}^{a,PMR} \\ C_{H_2O}^{a,PMR} \\ C_{CO}^{a,PMR} \\ C_{H_2}^{a,PMR} \\ C_{CO_2}^{a,PMR} \\ C_{Ar}^{a,PMR} \end{bmatrix}, \quad \boldsymbol{F_0^{a,PMR}} = \begin{bmatrix} F_{CH_4,0}^{a,PMR} \\ F_{H_2O,0}^{a,PMR} \\ F_{CO,0}^{a,PMR} \\ F_{H_2,0}^{a,PMR} \\ F_{CO_2,0}^{a,PMR} \\ F_{Ar,0}^{a,PMR} \end{bmatrix}, \quad \boldsymbol{R} = \begin{bmatrix} -r_1 W_{cat} \\ (-r_1 - r_2) W_{cat} \\ r_1 W_{cat} \\ (3r_1 + r_2) W_{cat} \\ -r_2 W_{cat} \\ 0 \end{bmatrix}, \quad \boldsymbol{F_{ex}} = \begin{bmatrix} 0 \\ 0 \\ 0 \\ \frac{I_m}{2F_a} \\ 0 \\ 0 \end{bmatrix} \tag{45b}$$

where the dynamic behavior of species concentrations is captured by $\dot{\boldsymbol{C}}^{\boldsymbol{a,PMR}}$.

For the energy balance shown in Eq. (32), the net heat from the reaction term ($Q^{a,PMR}$) for the PMR process can be defined as:

$$Q^{a,PMR} = -r_1 W_{cat} \Delta H_1(T) - r_2 W_{cat} \Delta H_2(T) \tag{46}$$

where $\Delta H_1(T)$ and $\Delta H_2(T)$ are the heats of reaction for the SMR reaction (Eq. (22a)) and the WGS reaction (Eq. (22b)), respectively. These enthalpy changes are calculated based on their thermodynamic definitions:

$$\Delta H_1(T) = 3H_{H_2}(T) + H_{CO}(T) - H_{CH_4}(T) - H_{H_2O}(T) \tag{47a}$$

$$\Delta H_2(T) = H_{H_2}(T) + H_{CO_2}(T) - H_{CO}(T) - H_{H_2O}(T) \tag{47b}$$

where $H_{CH_4}(T)$, $H_{H_2O}(T)$, $H_{CO}(T)$, $H_{H_2}(T)$ and $H_{H_2O}(T)$ are the enthalpies of CH_4, H_2O, CO, H_2 and CO_2 as a function of the process temperature, respectively. These enthalpy values can be calculated by the Shomate equation (Shomate, 1944):

$$H_i(T) = \sum_{j=1}^{4} \frac{A_{i,j}}{j} T^j - \frac{A_{i,5}}{T} + A_{i,6} \tag{48}$$

Additionally, from thermodynamics, the derivative of the Shomate equation reveals the relationship between the heat capacity of a gas component as a function of the process temperature (T) at constant pressure ($C_{p,i}$) by taking the derivative of Eq. (48):

$$C_{p,i}(T) = \left(\frac{\partial H_i(T)}{\partial T}\right)_P = \sum_{j=1}^{4} A_{i,j} T^{j-1} + \frac{A_{i,5}}{T^2} \tag{49}$$

where $A_{j,i}$ for $i = 1, 2, \ldots, 6$ for species j are the constant coefficients of species j in the Shomate equation.

To determine the external heat source terms in Eqs. (32) and (37), considering the utilization of the electric furnace, the following expressions are developed:

$$Q_h^{a,PMR} = f_h^{a,PMR} I_f^2 R_f \tag{50a}$$

$$Q_h^{c,PMR} = f_h^{c,PMR} I_f^2 R_f \tag{50b}$$

where the $Q_h^{a,PMR}$ and $Q_h^{c,PMR}$ represent heat source terms of the anode (retentate) and the cathode (permeate). These terms are calculated from Joule's law. The $f_h^{a,PMR}$ and $f_h^{c,PMR}$ represent the fraction of source heat to the anode and cathode. However, in practice, $f_h^{a,PMR} + f_h^{c,PMR} < 1$ due to external heat loss to the surroundings of the process.

To determine the extraction heat ($\dot{Q}_e$) generated by electrochemical separation, a resistive-heating model is considered. The electric current that is applied to the PMR membrane to extract H_2 from the anode encounters a resistance which causes Joule-heating according to ($\dot{Q}_J$). Additionally, according to Malerød-Fjeld et al. (2017), the extracted H_2 is further compressed as it separates against a pressure gradient induced by a 30 bar pressure differential across the cathode and anode. Additional energy is generated by the compression process ($\dot{Q}_c$).

$$\dot{Q}_e = \dot{Q}_J + \dot{Q}_c \tag{51}$$

The heats of extraction and compression are defined as follows (Malerød-Fjeld et al., 2017):

$$\dot{Q}_J = I_m^2 R_m \tag{52a}$$

$$\dot{Q}_c = F_{H_2,ex} R T^{c,PMR} \ln\left(\frac{P^{c,PMR}}{P^{a,PMR}}\right) \tag{52b}$$

Considering the extraction heat occurring on the solid oxide interface located between the anode and the cathode, the total extraction heat is split into two parts, as follows:

$$\dot{Q}_e^{a,PMR} = f_e^{a,PMR} \dot{Q}_e \tag{53a}$$

$$\dot{Q}_e^{c,PMR} = f_e^{c,PMR} \dot{Q}_e \tag{53b}$$

$$f_e^{a,PMR} + f_e^{c,PMR} = 1 \tag{53c}$$

where $f_e^{a,PMR}$ and $f_e^{c,PMR}$ are fractions of the extraction heat contributing to the anode and cathode. In this model, the same heat contribution from both sides of the membrane is assumed:

$$f_e^{a,PMR} = f_e^{c,PMR} = \frac{1}{2} \tag{54}$$

For a PMR system, both the anode and cathode are enclosed within a furnace and heat insulation material. It is therefore reasonable to assume that the two sides of the reactor maintain approximately the same temperature, leading to negligible heat transfer:

$$T^{a,PMR} \approx T^{c,PMR} \tag{55a}$$

$$\dot{Q}_c^{a,PMR} \approx \dot{Q}_a^{c,PMR} \approx 0 \tag{55b}$$

where $\dot{Q}_c^{a,PMR}$ and $\dot{Q}_a^{c,PMR}$ represent the heat transfer rate from the cathode to anode and the heat transfer rate from the anode to cathode, respectively.

Based on Eqs. (32), (46), (50a), (51), (52), (53a), (54) and (55b), the dynamic temperature equation for the anode can be calculated with the following equation:

$$\dot{T}^{a,PMR} = \frac{f_h^{a,PMR} I_f^2 R_f + \sum F_{i,0}^{a,PMR} \int_{T_0^{a,PMR}}^{T^{a,PMR}} C_{p,i}\, dT' - r_1 W_{cat} \Delta H_1(T^{a,PMR}) - r_2 W_{cat} \Delta H_2(T^{a,PMR})}{\sum \rho_i^{a,PMR} C_{p,i} V^{a,PMR}} + \frac{U_h^{a,PMR} A_h^{a,PMR} (T^a - T^{a,PMR}) + \frac{1}{2} I_m^2 R_m + \frac{I_m}{4F_a} R T^{a,PMR} \ln\left(\frac{P^{c,PMR}}{P^{a,PMR}}\right)}{\sum \rho_i^{a,PMR} C_{p,i} V^{a,PMR}} \tag{56}$$

where $i = CH_4, H_2O, CO, H_2, CO_2, Ar$.

Similarly, for the cathode, based on Eqs. (36) and (40), the total volumetric flowrate (q_c) is calculated as follows:

$$q^{c,PMR} = \left(\sum F_{l,0}^{c,PMR} + \frac{I_m}{2F_a}\right) \frac{R T^{c,PMR}}{P^{c,PMR}} + \frac{V^{c,PMR}}{T^{c,PMR}} \dot{T}^{c,PMR} \tag{57}$$

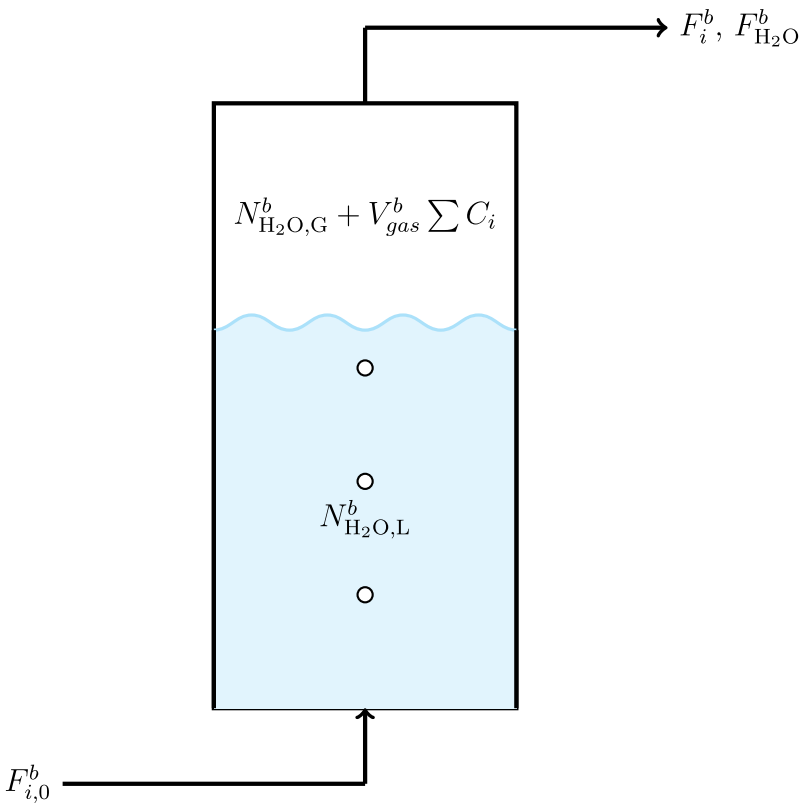

Fig. 4. Schematic describing the molar flow of the anodic dry gas mixture passing through the bubbler apparatus to generate a humidified wet mixture of CH_4 and H_2 reactants.

According to Eqs. (34) and (40), the dynamic model for gas species concentrations in the cathode is given by the following equation:

$$\dot{\boldsymbol{C}}^{\boldsymbol{c,PMR}} = \frac{1}{V^{c,PMR}} \left(\boldsymbol{F}_{\boldsymbol{0}}^{\boldsymbol{c,PMR}} - q^{c,PMR} \boldsymbol{C}^{\boldsymbol{c,PMR}} + \boldsymbol{F}_{\boldsymbol{ex}} \right) \tag{58a}$$

$$\boldsymbol{C}^{\boldsymbol{c,PMR}} = \begin{bmatrix} C_{\mathrm{H_2O}}^{c,PMR} \\ C_{\mathrm{H_2}}^{c,PMR} \end{bmatrix}, \quad \boldsymbol{F}_{\boldsymbol{0}}^{\boldsymbol{c,PMR}} = \begin{bmatrix} F_{\mathrm{H_2O},0}^{c,PMR} \\ F_{\mathrm{H_2},0}^{c,PMR} \end{bmatrix}, \quad \boldsymbol{F}_{\boldsymbol{ex}} = \begin{bmatrix} 0 \\ \frac{I_m}{2F_a} \end{bmatrix} \tag{58b}$$

Based on Eqs. (37), (50b). (51), (52b), (53b), (54) and (55b), the energy balance for the cathode is defined as:

$$\begin{aligned} \dot{T}^{c,PMR} = & \frac{f_h^{c,PMR} I_m^2 R_f + \sum F_{i,0}^{c,PMR} \int_{T_0}^{T^{c,PMR}} C_{p,i}\, dT' + \frac{I_m}{2F_a} \int_{T^{a,PMR}}^{T^{c,PMR}} C_{p,\mathrm{H_2}}\, dT'}{\sum \rho_i^{c,PMR} C_{p,i} V^{c,PMR}} \\ & + \frac{U_h^{c,PMR} A_h^{c,PMR} (T^a - T^{c,PMR}) + \frac{1}{2} I_m^2 R_m + \frac{I_m}{4F_a} R T^{c,PMR} \ln\left(\frac{P^{c,PMR}}{P^{a,PMR}}\right)}{\sum \rho_i^{c,PMR} C_{p,i} V^{c,PMR}} \end{aligned} \tag{59}$$

Therefore, the dynamic first principles model state for the PMR can be expressed as:

$$\boldsymbol{x}^{\boldsymbol{PMR}} = \begin{bmatrix} \boldsymbol{C}^{\boldsymbol{a,PMR}} \\ T^{a,PMR} \\ \boldsymbol{C}^{\boldsymbol{c,PMR}} \\ T^{c,PMR} \end{bmatrix} \tag{60}$$

3.3. Bubbler model

A bubbler is commonly used in gas-phase systems to generate steam, functioning as an efficient vaporizer for liquids such as water. The primary steam generation mechanism involves passing dry gases through a liquid reservoir at a controlled temperature. As the gas stream bubbles through the liquid, it facilitates the transfer of the vapor phase, steam in this case, into the gas stream. This process is highly effective for generating a consistent and controlled amount of steam, as the rate of vaporization can be modulated by adjusting the bubbler's temperature, flowrate of the carrier gas or gas stream, or system pressure. The use of a bubbler for steam generation is particularly advantageous due to its simplicity and ability to precisely control the partial pressure of gas-phase steam, which is critical in industrial-scale chemical reactions and materials processing.

In Fig. 4, a schematic of the anode bubbler is illustrated. Based on Dolton's law, the steam flowrate exiting the bubbler ($F_{\mathrm{H_2O}}^b$) can be estimated from the steam partial pressure (P_s^b):

$$F_{\mathrm{H_2O}}^b = \frac{\sum F_{i,0}^b}{P^b - P_s^b} P_s^b, \quad i = \mathrm{CH_4}, \mathrm{H_2} \tag{61}$$

The steam partial pressure can be calculated using the Antoine equation (Thomson, 1946):

$$\log_{10}(P_s^b) = A_a - \frac{B_a}{T^b + C_a} \tag{62}$$

where A_a, B_a and C_a are constant parameters for water. From Eq. (62), the P_s^b is directly influenced by the bubbler temperature (T^b). To investigate the dynamic change of the bubbler temperature, an energy balance is applied to a general bubbler model, as shown in Eq. (63):

$$\dot{T}^b = \frac{\dot{Q}^b - \sum F_{i,0}^b \int_{T_0^b}^{T^b} C_{p,j} dT' + U^b A^b (T^a - T^b)}{N_{H_2O,L}^b M_{H_2O} C_{p,H_2O} + V_{gas}^b \sum \rho_j^b C_{p,j}} \tag{63}$$

where $\dot{Q}^b$ represents the heat supply to the bubbler that is modulated to vary the bubbler's temperature. Steam continuously exits the bubbler causing a gradual decrease in the liquid water level in the bubbler tank ($N_{H_2O,L}^b$) and requires a mole balance to account for the change of $N_{H_2O,L}^b$.

Within the bubbler, H_2O exists in a gas phase ($N_{H_2O,G}^b$) and a liquid phase ($N_{H_2O,L}^b$):

$$N_{H_2O}^b = N_{H_2O,L}^b + N_{H_2O,G}^b \tag{64}$$

where $N_{H_2O}^b$ is denoted as the total moles of water inside the bubbler. Moles of water in the gas phase, can be calculated by the following equations:

$$N_{H_2O,G}^b = C_{H_2O}^b V_G^b \tag{65a}$$

$$C_{H_2O}^b = \frac{P_s^b}{T^b R} \tag{65b}$$

$$V_{gas}^b = V^b - \frac{N_{H_2O,L}^b M_{H_2O}}{\rho_{H_2O}} \tag{65c}$$

where the concentration of H_2O ($C_{H_2O}^b$) is calculated by the ideal gas law, and the total gas-phase volume (V_G^b) is the difference of the total bubbler volume and the liquid-phase volume. Therefore, the overall H_2O mole balance for the bubbler follows:

$$\begin{aligned}
\dot{N}_{H_2O}^b &= \frac{d}{dt}\left(N_{H_2O,L}^b + \frac{P_s^b}{T^b R}\left(V^b - \frac{N_{H_2O,L}^b M_{H_2O}}{\rho_{H_2O}}\right)\right) \\
&= \frac{dN_{H_2O,L}^b}{dt} + \frac{1}{R}\frac{d\left(\frac{P_s^b}{T^b}\right)}{dt}\left(V^b - \frac{N_{H_2O,L} M_{H_2O}}{\rho_{H_2O}}\right) - \frac{M_{H_2O}}{R\rho_{H_2O}}\frac{P_s^b}{T^b}\frac{dN_{H_2O,L}^b}{dt} \\
&= \left(1 - \frac{M_{H_2O}}{R\rho_{H_2O}}\frac{P_s^b}{T^b}\right)\frac{dN_{H_2O,L}^b}{dt} + \left(\frac{V^b}{R} - \frac{N_{H_2O,L} M_{H_2O}}{R\rho_{H_2O}}\right)\frac{d\left(\frac{P_s^b}{T^b}\right)}{dt} = -F_{H_2O}^b
\end{aligned} \tag{66}$$

Assume $\lambda^b = \frac{P_s^b}{T^b}$, so $\dot{\lambda}^b = \frac{d\left(\frac{P_s^b}{T^b}\right)}{dt}$ can be calculated via Eq. (67).

$$\dot{\lambda}^b = \frac{\partial \lambda^b}{\partial T^b}\dot{T}^b \tag{67}$$

where $\frac{\partial \lambda^b}{\partial T^b}$ can be calculated as follows:

$$\frac{\partial \lambda^b}{\partial T^b} = \left(\ln(10) \cdot \left(\frac{B_a}{(T^b + C_a)^2}\right) \cdot T^b - 1\right) \cdot \frac{P_s^b}{(T^b)^2} \tag{68}$$

Based on Eqs. (61), (66) and (67), the expression of the liquid water inside the bubbler can be presented as:

$$\dot{N}_{H_2O,L} = \frac{\left(\frac{N_{H_2O,L} M_{H_2O}}{R\rho_{H_2O}} - \frac{V^b}{R}\right)\dot{\lambda}^b - \frac{P_s^b \sum F_{i,0}^b}{P^b - P_s^b}}{1 - \frac{P_s^b M_{H_2O}}{RT^b \rho_{H_2O}}} \tag{69}$$

For most cases, $\frac{P_s^b M_{H_2O}}{RT^b \rho_{H_2O}} \ll 1$. Therefore, this equation can be simplified to:

$$\dot{N}_{H_2O,L} \approx \left(\frac{N_{H_2O,L} M_{H_2O}}{R\rho_{H_2O}} - \frac{V^b}{R}\right)\dot{\lambda}^b - \frac{P_s^b \sum F_{i,0}^b}{P^b - P_s^b} \tag{70}$$

Thus, the first principles model state for the bubbler can be expressed as:

$$\boldsymbol{x^b} = \begin{bmatrix} T^b \\ N_{H_2O,L} \end{bmatrix} \tag{71}$$

and the overall first principles model state for the PMR system can be expressed as:

$$\boldsymbol{x_{fp}} = \begin{bmatrix} \boldsymbol{x^{PMR}} \\ \boldsymbol{x^b} \end{bmatrix} \tag{72}$$

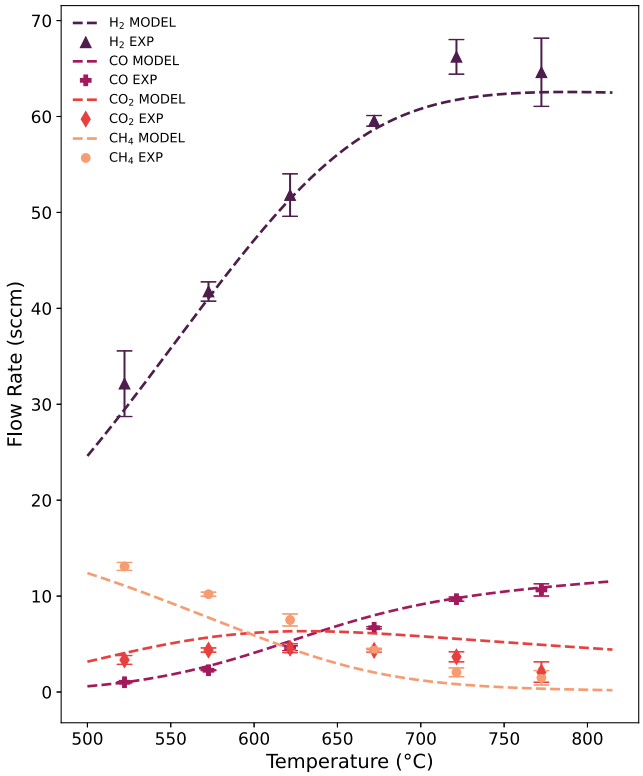

Fig. 5. Steady state anode gas compositions without hydrogen separation for the PMR model and experiments at 1 bar. Error bars represent the standard deviations of five GC measurements at every steady state temperature.

3.4. PMR model validation

The first principles model for the PMR process ($\boldsymbol{x}^{PMR}$) was validated by comparing experimental data with the corresponding simulation results for SMR with and without electrochemical H_2 extraction. To validate the steady state solutions for the dynamic PMR model, the reformer operating temperature was incrementally increased from 522 to 772 °C in the absence of an electric current. Fig. 5 provides the gas product composition for six steady state temperatures throughout the PMR operating range, and the process model was fitted to the experimentally generated data by choosing the catalyst weight parameter that minimized the error between the model predictions for gas species exiting the reactor and the observed species compositions measured by the GC. Using 66 mg as the active catalyst weight, the volumetric flowrates of H_2 and CO align with the PMR model predictions. However, the model overpredicts the consumption of CH_4 and the generation of CO_2 by 1–2 sccm on average. Given the CH_4 and CO_2 absolute errors are within the range of experimental measurement error, and the model calculations and observed volumetric flowrates follow the same trend in response to a reactor temperature change, the PMR process model is sufficiently predictive for MPC applications.

After fitting the steady state data to the PMR model for the zero-extraction case, and to test the transient accuracy of the PMR model, a dynamic experiment was conducted to supply 0 to 8 A of current from the potentiostat to the PMR unit. Fig. 6 validates the PMR application of the CST-MR model, the H_2 extraction rate correlation, and the reactor temperature model derived from the PMR energy balance. The underprediction of the H_2 generation rate was 6 sccm, on average, for all currents. It is thought that the catalytic performance of the membrane improved from the initial steady state experiments due to the further reduction of NiO surface sites during the reactor downtime in pure H_2 and 400 °C anode gas stream conditions. The underprediction of H_2 extraction into the cathode likely originated from measurement drift in the flow sensor as a consequence of a sluggish thermocouple in the sensing device. Still, the deviations are within the expected experimental error, and the dynamics of the reactor process variables closely align with the overall kinetic, extraction, and energy dynamics of the PMR model (Fig. 6).

4. Feedback controller design and results

In this section, feedback controllers are designed to address realistic challenges encountered in industrial chemical production plants, such as practical input constraints, controller response speed, computational costs, and common process disturbances. In the feedback control simulations, the experimental conditions listed in the model validation exercise are adjusted to reflect the industrial implementation of the PMR system. The initial operating conditions for computational feedback control are as follows: 20 sccm of $F_{CH_4,0}^{a,PMR}$ and 12.5 sccm of $F_{H_2,0}^{a,PMR}$ are sent to the anode bubbler, while 10 sccm of $F_{H_2,0}^{c,PMR}$ is sent to the cathode bubbler. Each bubbler is assumed to have a 1 liter total volume with 80% of the total volume being liquid-phase water. The temperatures of both bubblers are 157 °C and 227 °C for the anode and cathode, respectively. These bubbler temperatures correspond to 60% and 66.7% steam mixtures according to Eqs. (61) and (62). Heating rates of 67.7 W and 98.6 W are needed to maintain these temperatures. The inlet temperatures of the reformer ($T_0^{a,PMR}, T_0^{c,PMR}$) are both 735 °C, and the temperatures inside the reformer are 788 °C and 813 °C for the anode and cathode, respectively. To compress hydrogen upon separation, the anode pressure is 10 bar and the cathode pressure is 40 bar. For the first 5 min of each control simulation, all process variables are at steady state and the controllers are inactive. After $t = 5$ min, the controllers are activated.

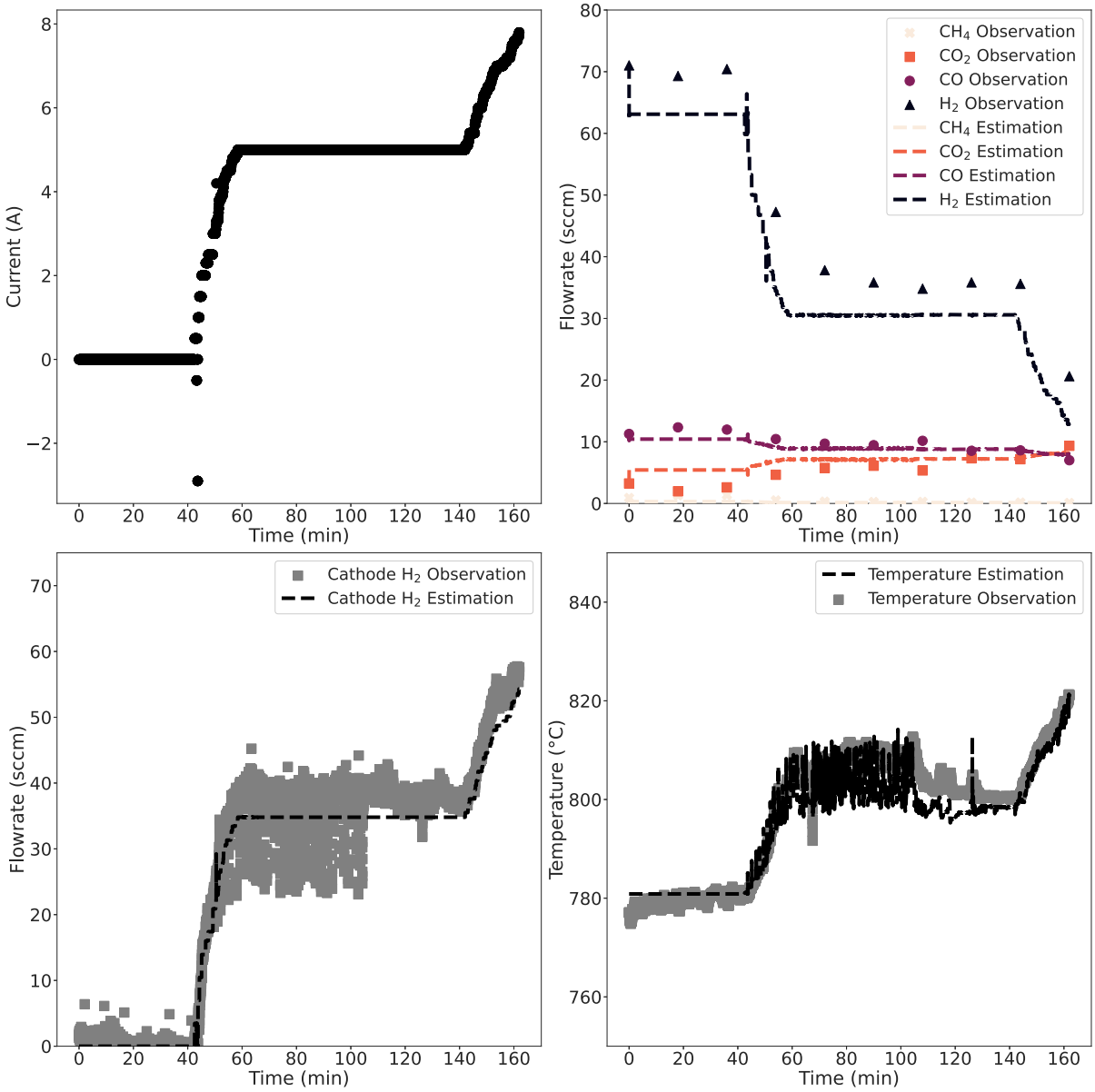

Fig. 6. Comparison of the PMR model predictions with dynamic experimental data at 1 bar with an initial reactor temperature of 777 °C.

4.1. Control scenario

In a practical PMR process, the cathode hydrogen flowrate ($F_{H_2}^{c,PMR}$), representing the extracted and collected hydrogen product, must be regulated. Experimentally, $F_{H_2}^{c,PMR}$ can be directly measured by the digital flowmeter discussed in Section 2.7.2, providing real time feedback for control. Only the H_2 extracted ($F_{H_2,ex}$) through the membrane is used as the control target, so the inlet H_2 in the cathode is subtracted from the sensor reading:

$$F_{H_2,ex} = F_{H_2}^{c,PMR} - F_{H_2,0}^{c,PMR} \tag{73}$$

In the model, the control target can be estimated by transforming the state variables as follows:

$$\hat{F}_{H_2,ex} = \hat{q}^{c,PMR}\hat{C}_{H_2}^{c,PMR} - F_{H_2,0}^{c,PMR} \tag{74}$$

where $\hat{q}^{c,PMR}$ and $\hat{C}_{H_2}^{c,PMR}$ are the estimated volumetric flowrate and H_2 concentration in the cathode. In industry, hydrogen production setpoints are selected for economic optimization. For the experimental case, a 120 sccm production rate is assumed to be the optimal value of $F_{H_2,ex}$ and the target setpoint ($F_{H_2,ex,sp} = 120$ sccm).

Another key parameter in this process is hydrogen recovery (HR). HR is defined as the percentage of the extracted H_2 to the theoretical maximum H_2 ($F_{H_2,max}$) that can be recovered. In the case of the PMR system, $F_{H_2,max}$ is the sum of the extracted hydrogen flow ($F_{H_2,ex}$) and the

hydrogen contained in the anode exhaust gas ($F_{H_2}^{a,PMR}$). Therefore:

$$HR = \frac{F_{H_2,ex}}{F_{H_2,max}} \cdot 100\% = \frac{F_{H_2,ex}}{F_{H_2}^{a,PMR} + F_{H_2,ex}} \cdot 100\% \tag{75}$$

Attaining a high HR is critical for optimal H_2 extraction and for minimal H_2 product loss to the anode exhaust stream. The removal of anodic H_2 also shifts the reaction (Eq. (22)) equilibrium towards enhanced conversion of reactants such as CO and CH_4. In the simulation, a HR setpoint of 98% is chosen ($HR_{sp} = 98\%$), and $F_{H_2}^{a,PMR}$ is measured in real time using an automated GC with an 18-min sampling interval and a 15-min delay, as described in Section 2.7.2. Additionally, the $F_{H_2,ex}$ is measured and calculated with a digital flow meter and Eq. (73) for real time feedback.

By combining Eq. (74), the HR is estimated by transforming the process state variables in the following manner:

$$HR = \frac{\hat{F}_{H_2,ex}}{\hat{F}_{H_2,max}} \cdot 100\% = \frac{\hat{q}^{c,PMR}\hat{C}_{H_2}^{c,PMR} - F_{H_2,0}^{c,PMR}}{\hat{q}^{a,PMR}\hat{C}_{H_2}^{a,PMR} + \hat{q}^{c,PMR}\hat{C}_{H_2}^{c,PMR} - F_{H_2,0}^{c,PMR}} \cdot 100\% \tag{76}$$

Except for $F_{H_2,ex}$ and HR, the steam inlet flowrate ($F_{H_2O,0}^{a,PMR}$) plays a pivotal role in the PMR process, as an increased flowrate shifts the equilibrium of both the SMR (Eq. (22a)) and WGS (Eq. (22b)) reactions, leading to enhanced conversion of CO and CH_4. Moreover, a higher steam flowrate improves membrane conductivity by ensuring sufficient hydration, as demonstrated by Malerød-Fjeld et al. (2017). Additionally, the S/C ratio effectively mitigates carbon deposition on the catalyst, a prevalent issue in SMR processes (Meloni et al., 2020; Jeon et al., 2018). On the other hand, excessive steam dilutes the reactants, lowering their partial pressures and reducing the overall reaction rate. To balance this phenomenon, the S/C ratio, defined as the ratio of inlet steam to methane flowrates, is regulated:

$$S/C = \frac{F_{H_2O,0}^{a,PMR}}{F_{CH_4,0}^{a,PMR}} \tag{77}$$

An S/C ratio of 2.5 is targeted to balance these effects ($S/C_{sp} = 2.5$). This ratio ensures sufficient anodic steam to simultaneously drive reactant conversion and maintain membrane conductivity. Thus, precise control of the S/C ratio is crucial for optimizing thermal and electrochemical reaction performance.

However, the S/C ratio cannot be directly measured. Instead, the bubbler temperature (T^b), measured by a thermocouple inside the bubbler, is used as a proxy for this measurement. Therefore, the relationship between the bubbler temperature and S/C must be developed, with S/C_{sp} and $T_{b,sp}$ representing the setpoint of S/C and T^b, respectively. Based on Eq. (62), the setpoint bubbler temperature can be determined from the steam fraction under the S/C setpoint in the bubbler ($\Lambda_{H_2O,sp}^b = f(S/C_{sp})$):

$$T_{b,sp} = \frac{B_a}{A_a - \log_{10}(P^b \cdot \Lambda_{H_2O,sp}^b)} - C_a \tag{78}$$

where the $\Lambda_{H_2O,sp}^b$ can be calculated based on Eqs. (61) and (77):

$$\Lambda_{H_2O,sp}^b = \frac{S/C_{sp} \cdot F_{CH_4,0}^{a,PMR}}{S/C_{sp} \cdot F_{CH_4,0}^{a,PMR} + F_{CH_4,0}^{a,PMR} + \sum F_{i,0}^{a,PMR}} \tag{79}$$

where $i = CO, H_2, CO_2$. Therefore, to achieve the desired S/C ratio, the required bubbler temperature is set.

Overall, based on these considerations, the control target vector ($\boldsymbol{y}$) is defined as follows:

$$\boldsymbol{y} = \begin{bmatrix} y_1 \\ y_2 \\ y_3 \end{bmatrix} = \begin{bmatrix} F_{H_2,ex} \\ HR \\ T^b \end{bmatrix} \tag{80}$$

The overall control objective is to reach the control target setpoint ($\boldsymbol{y_{sp}}$) from the initial steady state values ($\boldsymbol{y}(0) = \begin{bmatrix} 0 & 0 & 157\,°C \end{bmatrix}^\top$), by manipulating the control input vector ($\boldsymbol{u}$), which is defined in Eq. (81).

$$\boldsymbol{u} = \begin{bmatrix} u_1 \\ u_2 \\ u_3 \end{bmatrix} = \begin{bmatrix} F_{CH_4,0}^{a,PMR} \\ I_m \\ \dot{Q}^b \end{bmatrix} \tag{81}$$

Specifically, $F_{CH_4,0}^{a,PMR}$, I_m and $\dot{Q}_h$ are manipulated via the flow indicator, potentiostat, and heater to the bubbler. The corresponding initial control input vector is $\begin{bmatrix} 20\ \text{sccm} & 0 & 67.7\ \text{W} \end{bmatrix}$.

In this control framework, three closed-loop subsystems have been established. The first subsystem aims to achieve the desired $F_{H_2,ex}$ (y_1) by adjusting the input $F_{CH_4,0}^{a,PMR}$ (u_1). The first subsystem consists of a CH_4 mass flow controller as the actuator and sensor in the feedback loop that considers the PMR and bubbler units as the process. The second subsystem is designed to attain the target hydrogen recovery rate HR (y_2) through the modulation of the electric current input I_m (u_2). In the second subsystem, the GC and digital flowmeter are feedback sensors, while the potentiostat serves as the actuator in this subsystem that only considers the PMR process. The third subsystem focuses on reaching the specified bubbler temperature T^b (y_3) by controlling the heat input $\dot{Q}^b$ (u_3). The T^b is measured by a thermocouple, while the heat input is provided by resistive-heating tape around the bubbler. This subsystem only considers the bubbler as the closed-loop process.

Remark 3. From Eq. (79), $\Lambda_{H_2O,sp}^b = f(S/C_{sp})$ varies with the manipulation of $F_{CH_4,0}^{a,PMR}$ under the same S/C ratio. Therefore, the setpoint of the bubbler temperature varies with time throughout the control run ($T_{b,sp} = T_{b,sp}(t)$).

Remark 4. The three defined subsystems are interdependent. Specifically, within the first control subsystem, the control target $F_{H_2,ex}$ cannot be directly adjusted by $F_{CH_4,0}^{a,PMR}$. Instead, $F_{CH_4,0}^{a,PMR}$ influences the total generation of H_2 by thermal reactions, thereby altering the HR as defined in Eq. (75). To achieve the desired level of HR, the current (I_m) adjusts accordingly, which in turn modifies $F_{H_2,ex}$ to reach the setpoint.

4.2. Control input constraints

Control input constraints are considered in this study to ensure safety, stability, cost-effectiveness, and efficiency. For $F_{CH_4,0}^{a,PMR}$, a low methane inlet flowrate leads to slow hydrogen generation, while an excessively high flowrate results in unreacted methane being lost in the exhaust stream due to insufficient reaction time. To address this, the methane flowrate is constrained by the residence time (or space time, τ) of the reformer, ensuring an optimal balance between hydrogen production and methane utilization. Since the reaction only takes place in the anode, the τ is defined as the anode volume divided by the anodic volumetric flowrate, which indicates the average time the reactant gases remain inside the reaction control volume.

$$\tau = \frac{V^{a,PMR}}{q_0^{a,PMR}} \tag{82}$$

Combining the ideal gas law, the $q_0^{a,PMR} = f(F_{CH_4,0}^{a,PMR})$ relation is determined by Eq. (83):

$$\begin{aligned} q_0^{a,PMR}(t) &= \frac{\sum F_{i,0}^{a,PMR} + F_{H_2O,0}^{a,PMR}(t) + F_{CH_4,0}^{a,PMR}(t)}{\sum C_{i,0}^{a,PMR}} \\ &= \left(\sum F_{i,0}^{a,PMR} + F_{H_2O,0}^{a,PMR}(t) + F_{CH_4,0}^{a,PMR}(t)\right) \frac{RT_0^{a,PMR}}{P^{a,PMR}} \end{aligned} \tag{83}$$

where $i = CO, H_2, CO_2, Ar$, represents the constant inlet gas species and $j = CH_4, H_2O, CO, H_2, CO_2, Ar$, represents all inlet gas species. The minimum and maximum residence times are defined as τ_{min} and τ_{max}. According to Eqs. (82) and (83), the feasible operating region U_1 of $F_{CH_4,0}^{a,PMR}(t)$ is defined as follows:

$$U_1 = \left\{ F_{CH_4,0}^{a,PMR}(t) \,\middle|\, F_{CH_4,0,\min}^{a,PMR}(t) \le F_{CH_4,0}^{a,PMR}(t) \le F_{CH_4,0,\max}^{a,PMR}(t), \quad \forall t \in [0,\infty) \right\} \tag{84a}$$

$$F_{CH_4,0,\min}^{a,PMR}(t) = \frac{V^{a,PMR} P^{a,PMR}}{\tau_{\max} R T_0^{a,PMR}} - \sum F_{i,0}^{a,PMR} - F_{H_2O,0}^{a,PMR}(t) \tag{84b}$$

$$F_{CH_4,0,\max}^{a,PMR}(t) = \frac{V^{a,PMR} P^{a,PMR}}{\tau_{\min} R T_0^{a,PMR}} - \sum F_{i,0}^{a,PMR} - F_{H_2O,0}^{a,PMR}(t) \tag{84c}$$

where $F_{CH_4,0,\min}^{a,PMR}(t)$ and $F_{CH_4,0,\max}^{a,PMR}(t)$ represent the minimum and maximum limits of $F_{CH_4,0}^{a,PMR}(t)$ corresponding to τ_{max} and τ_{min}, respectively.

The membrane current (I_m) directly causes the rate of H_2 extraction seen in Eq. (40). However, this extraction rate must be constrained to ensure the safety of the entire process. For convenience and generality, these constraints are initially formulated within the CST-MR framework. Specifically, the volumetric flowrate and the concentration of the extracted species on the retentate side must remain positive:

$$q^r(t) \ge 0 \quad \forall t \in [0,\infty) \tag{85a}$$

$$C_k^r(t) \ge 0 \quad \forall t \in [0,\infty) \tag{85b}$$

The constraint in Eq. (85a) is achieved in Eq. (86)

$$\sum F_{k,rem}(t) \le \sum F_{k,rem,max,1}(t), \quad \forall t \in [0,\infty) \tag{86a}$$

$$\sum F_{k,rem,max,1}(t) = \sum F_{i,0}^r(t) + \sum R_{j,gen}(t) + \sum R_{k,gen}(t) + \frac{V^r}{T^r(t)} \dot{T}^r(t) \sum C_i^r(t) \tag{86b}$$

Therefore, the inequalities in Eqs. (86) and (85a) are satisfied by considering Eqs. (30) and (86),

$$\begin{aligned} q^r &= \left(\sum F_{i,0}^r(t) + \sum R_{j,gen}(t) + \sum R_{k,gen}(t) - \sum F_{k,rem}(t)\right) \frac{RT^r}{P^r} + \frac{V^r}{T^r(t)} \dot{T}^r(t) \\ &\ge \left(\sum F_{i,0}^r(t) + \sum R_{j,gen}(t) + \sum R_{k,gen}(t)\right) \frac{RT^r(t)}{P^r(t)} + \frac{V^r}{T^r(t)} \dot{T}^r(t) \\ &\quad - \left(\sum F_{i,0}^r(t) + \sum R_{j,gen}(t) + \sum R_{k,gen}(t) + \frac{V^r}{T^r(t)} \dot{T}^r(t) \sum C_i^r(t)\right) \frac{RT^r(t)}{P^r(t)} = 0 \end{aligned} \tag{87}$$

To ensure Eq. (85b), the constraint for $F_{k,rem}$ in Eq. (25b) can be rewritten as Eq. (88).

$$F_{k,rem}(t) \le F_{k,rem,max,2}(t), \quad \forall t \in [0,\infty) \tag{88a}$$

$$F_{k,rem,max,2}(t) = F_{k,0}^r(t) + R_{k,gen}(t) \tag{88b}$$

The satisfaction of Eqs. (88) and (85b) is as follows. Consider Eqs. (25b) and (88),

$$\begin{aligned} F_{k,0}^r(t) + R_{k,gen}(t) &= q^r\left(t, C_k^r(t)\right) C_k^r(t) + F_{k,rem}(t) + V^r \dot{C}_k^r(t) \\ &\le q^r\left(t, C_k^r(t)\right) C_k^r(t) + F_{k,0}^r(t) + R_{k,gen}(t) + V^r \dot{C}_k^r(t) \end{aligned} \tag{89}$$

from which the following condition is obtained:

$$0 \le q^r\left(t, C_k^r(t)\right) C_k^r(t) + V^r \dot{C}_k^r(t) \tag{90}$$

This equation can be rearranged as follows:

$$0 \le \frac{q^r\left(t, C_k^r(t)\right)}{V^r} C_k^r(t) + \dot{C}_k^r(t) \tag{91}$$

Let $a(t)$ be defined as:

$$a(t) = \frac{q^r\left(t, C_k^r(t)\right)}{V^r} \tag{92}$$

since $q^r\left(t, C_k^r(t)\right) \ge 0$ (Eq. (85a)), $a(t) \ge 0$. Eq. (91) can be written as:

$$\dot{C}_k^r(t) + a(t)\, C_k^r(t) \ge 0 \tag{93}$$

This differential equation is solved by using an integrating factor, defined as:

$$\mu(t) = \exp\left(\int_0^t a(s)\, ds\right) \tag{94}$$

The $\mu(t)$ is multiplied on both sides of Eq. (93):

$$\mu(t)\, \dot{C}_k^r(t) + \mu(t)\, a(t)\, C_k^r(t) \ge 0 \tag{95}$$

The left-hand side of the inequality is recognized as the derivative of $\mu(t)\, C_k^r(t)$, thus simplifying the inequality to:

$$\frac{d}{dt}\left[\mu(t)\, C_k^r(t)\right] \ge 0 \tag{96}$$

Both sides of this equation can be integrated from 0 to t as follows:

$$\mu(t)\, C_k^r(t) - \mu(0)\, C_k^r(0) \ge 0 \tag{97}$$

Since $\mu(0) = \exp\left(\int_0^0 a(s)\, ds\right) = 1$ and $C_k^r(0) \ge 0$:

$$C_k^r(t) \ge \frac{C_k^r(0)}{\mu(t)} \ge 0 \tag{98}$$

Therefore, the only condition under which $C_k^r(t) \to 0$ is that $F_{k,rem}(t) = F_{k,rem,max,2}(t)$ and $\mu(t) \to \infty$ (i.e., $q^r\left(t, C_k^r(t)\right) \to \infty$) as $t \to \infty$. Hence, Eq. (85b) is satisfied.

Constraints developed for the CST-MR in Eqs. (86) and (88) can be applied to the current through the membrane in the PMR system based on Eq. (40), Table 1, Eqs. (44) and (45), shown in Eq. (99).

$$U_2 = \left\{ I_m(t) \,\middle|\, 0 \le I_m(t) \le \min\left\{ I_{m,max,1}(t),\ I_{m,max,2}(t) \right\},\quad \forall t \in [0, \infty) \right\} \tag{99a}$$

$$I_{m,max,1}(t) = 2F_a\left(\sum F_{i,0}^{a,PMR}(t) + 2r_1(t)W_{cat} + \frac{P^{a,PMR}V^{a,PMR}}{R\left(T^{a,PMR}(t)\right)^2}\dot{T}^{a,PMR}(t)\right) \tag{99b}$$

$$I_{m,max,2}(t) = 2F_a\left(F_{\mathrm{H_2},0}^{a,PMR} + \left(3r_1(t) + r_2(t)\right)W_{cat}\right) \tag{99c}$$

The rate of heat to the bubbler is limited by the maximum allowable loading power ($\dot{Q}_{max}^b$), so the feasible region for $\dot{Q}^b$ is given by

$$U_3 = \left\{ \dot{Q}^b(t) \,\middle|\, 0 \le \dot{Q}^b(t) \le \dot{Q}_{\max}^b,\quad \forall t \in [0, \infty) \right\} \tag{100}$$

Considering Eqs. (84), (99), and (100), the feasible operating region for the control inputs (U) is defined as:

$$U = \left\{ \boldsymbol{u}(t) = \begin{bmatrix} F_{\mathrm{CH_4},0}^{a,PMR}(t) \\ I_m(t) \\ \dot{Q}^b(t) \end{bmatrix} \,\middle|\, \forall t \in [0, \infty),\ \begin{array}{c} F_{\mathrm{CH_4},0,\min}^{a,PMR}(t) \le F_{\mathrm{CH_4},0}^{a,PMR}(t) \le F_{\mathrm{CH_4},0,\max}^{a,PMR}(t), \\ 0 \le I_m(t) \le \min\left\{ I_{\mathrm{H_2},\max,1}(t),\ I_{\mathrm{H_2},\max,2}(t) \right\}, \\ 0 \le \dot{Q}^b(t) \le \dot{Q}_{b,\max} \end{array} \right\} \tag{101}$$

Here, the magnitude of the change in I_m for two consecutive steps must be constrained, since a sudden change in current will directly change the PMR reactor temperature, which may lead to catalyst deactivation depending on the magnitude of the instantaneous temperature change. Consequently, by limiting the absolute maximum of I_m, the shift in the overall reaction equilibrium due to H_2 separation is also limited. Therefore, constraints on the methane flowrate step change ($\Delta F_{\mathrm{CH_4},0}^{a,PMR}$) are set accordingly. Additionally, a limited step change of $F_{\mathrm{CH_4},0}^{a,PMR}$ ensures the stability of the entire PMR system. The heat input to the bubbler, $\Delta\dot{Q}^b$, is also constrained, since a small change in the bubbler temperature can result in significant changes to the S/C ratio and have destabilizing effects. Based on the aforementioned considerations, the control input rate of change is defined as follows:

$$\boldsymbol{u}(t_k) - \boldsymbol{\Delta u_{limit}} \le \boldsymbol{u}(t_{k+1}) \le \boldsymbol{u}(t_k) + \boldsymbol{\Delta u_{limit}} \tag{102}$$

where $\boldsymbol{\Delta u}_{\boldsymbol{limit}}^{\top} = \begin{bmatrix} \Delta u_{1,limit} & \Delta u_{2,limit} & \Delta u_{3,limit} \end{bmatrix} = \begin{bmatrix} \Delta F_{\mathrm{CH_4},0,limit}^{a,PMR} & \Delta I_{\mathrm{H_2},limit} & \Delta\dot{Q}_{b,limit} \end{bmatrix}$. Through multiple simulations, $\Delta F_{\mathrm{CH_4},0,limit}^{a,PMR}$, $\Delta I_{\mathrm{H_2},limit}$ and $\Delta\dot{Q}_{b,limit}$ are chosen as 0.1 sccm, 0.1 A and 2 W.

Remark 5. Eq. (85) specifies the theoretical constraints used in our computational analysis. Violations of Eq. (85) would cause changes in the volumetric flow direction and insufficient concentrations of extracted species, posing significant risks to the system.

4.3. Proportional–integral control and MPC

Proportional–integral (PI) control is widely used in industrial systems due to its simplicity and ease of implementation. A PI controller adjusts control actions based on the immediate error (the proportional term) and the accumulation of past errors (the integral term) in relation to the control target setpoint. The PI control formulation for each subsystem j is shown in Eq. (103):

$$u_j = u_{j,sp} + K_{j,p} \cdot \left(y_{j,sp} - y_j\right) + K_{j,I} \int_0^t \left(y_{j,sp} - y_j\right) \, \mathrm{d}t' \quad \text{for } j = 1, 2, 3 \tag{103}$$

where $K_{j,P}$ and $K_{j,I}$ represent the proportional gain and the integral gain for each control loop j, respectively, both of which require tuning for optimal performance. In this simulation, the Ziegler–Nichols tuning method was employed for the determination of the controller tuning parameters. In the context of the PMR reactor controller, $K_{j,P}$ and $K_{j,I}$ are the proportional gain constants for each control loop, and are not to be confused with the equilibrium constants K_j for the SMR and WGS reactions used in the description of reaction kinetics. The control target setpoint vector is $\boldsymbol{y}_{\boldsymbol{sp}}^{\top} = \begin{bmatrix} y_{1,sp} & y_{2,sp} & y_{3,sp} \end{bmatrix} = \begin{bmatrix} F_{\mathrm{H}_2,ex,sp} & HR_{sp} & T_{b,sp} \end{bmatrix}$, and the corresponding control input setpoint vector is $\boldsymbol{u}_{\boldsymbol{sp}}^{\top} = \begin{bmatrix} u_{1,sp} & u_{2,sp} & u_{3,sp} \end{bmatrix} = \begin{bmatrix} F_{\mathrm{CH}_4,0,sp}^{a,PMR} & I_{\mathrm{H}_2,sp} & \dot{Q}_{b,sp} \end{bmatrix}$, where $j = 1, 2, 3$.

Despite its widespread applicability, PI control has several drawbacks, including slow response time and a limited ability to handle complex system constraints. To address these limitations, a model predictive control strategy is implemented in this work to achieve the desired control targets ($\boldsymbol{y}_{\boldsymbol{sp}}$) by manipulating the control inputs ($\boldsymbol{u}$), while considering the constraints developed in Section 4.2. The formulation for this MPC scheme is shown in Eq. (3). Specifically, $\hat{\boldsymbol{x}}$ is the state vector of the first principles model, $\boldsymbol{x}_{\boldsymbol{fp}}$, defined in Eq. (72). $\hat{\boldsymbol{F}}(\cdot)$ represents the first principles model developed in Section 3. $\hat{\boldsymbol{y}}$ refers to the estimation vector of $\boldsymbol{y}$ defined in Eq. (80). $\boldsymbol{h}(\cdot)$ describes the function vector transforming the $\boldsymbol{x}_{\boldsymbol{fp}}$ to $\hat{\boldsymbol{y}}$, developed in Section 4.1. Constraints of control input (U and $\boldsymbol{\Delta u}_{\boldsymbol{limit}}$) are defined in Eqs. (101) and (102), respectively.

To solve the optimization problem in real time, the sequential quadratic programming (SQP) approach is used to iteratively solve a series of quadratic programming subproblems, thereby decreasing the computational load during solution convergence (Boggs and Tolle, 1995). In Python, the SQP can be utilized from the "scipy" package.

The results are illustrated in Fig. 7, with the PI control simulation shown as the grey curve and the MPC control curve shown in purple. Initially, the control inputs are directly driven to the reference input setpoints for the PI controllers. In contrast, even though I_m and $\dot{Q}^b$ increase, $F_{\mathrm{CH}_4,0}^{a,PMR}$ in the MPC simulation decreases from 20 sccm to 15.9 sccm. This control action discrepancy originates from differences in the control methodologies of the two algorithms. The PI approach treats each subsystem independently, while the MPC approach is guided by a rigorous optimization framework. During the first few moments of control action for the CMPC scheme, even though more H_2 can be produced by increasing $F_{\mathrm{CH}_4,0}^{a,PMR}$, there is enough H_2 available for extraction in the PMR anode, and the centralized predictive controller sees no initial benefit for more $F_{\mathrm{H}_2,ex}$ by increasing $F_{\mathrm{CH}_4,0}^{a,PMR}$. The lower $F_{\mathrm{CH}_4,0}^{a,PMR}$, in the CMPC scheme, increases the S/C ratio in the anode based on Eq. (79), and decreases the bubbler temperature setpoint ($T_{b,sp}$) based on Eq. (78). These factors are considered in the MPC optimization problem, even though the CMPC scheme eventually increases both the methane flowrate and anodic bubbler temperature to the control target setpoints.

Although both controllers eventually reach the desired setpoints, the MPC algorithm significantly outperforms PI control in terms of response time. The predictive controller achieves a settling time of 25 min for the H_2 extraction flowrate ($F_{\mathrm{H}_2,ex,sp}$), 22 min for hydrogen recovery (HR_{sp}), and 25 min for the bubbler temperature (T_{sp}^b). In contrast, the PI controller requires 375 min, 70 min, and 587 min, respectively, to reach the same setpoints. This substantial reduction in settling time to steady state demonstrates the superior ability of MPC to handle system dynamics efficiently, making it a more effective control strategy for processes requiring rapid response and precise regulation. Additionally, MPC ensures that control inputs remain within the defined operating region, a guarantee that PI control cannot provide.

Remark 6. The PI control parameters, $K_{j,P}$ and $K_{j,I}$, are tuned not only to reach the setpoints without overshoot but also to ensure that all control inputs remain within the feasible constraints. This tuning leads to a significantly more attenuated response for the PI controller, which further contributes to its slower settling times compared to the MPC scheme. Also, the satisfaction of PI control constraints cannot be guaranteed, especially in practice.

4.4. Decentralized MPC

To facilitate real time implementation, a decentralized MPC approach is adopted to simplify the optimization problem, which reduces the time to solve the optimal control inputs. To do this, the whole system is divided to 3 subsystems, which is shown in Section 4.1. Based on the designated subsystems, and considering the relationships between $F_{\mathrm{CH}_4,0}^{a,PMR}$ and $F_{\mathrm{H}_2,ex}$, I_m and HR, $\dot{Q}^b$ and T^b, models for subsystem 1, 2 and 3 are defined as the following: $\boldsymbol{x_1} = \boldsymbol{x}_{\boldsymbol{fp}}$, $\boldsymbol{x_2} = \boldsymbol{x}^{\boldsymbol{PMR}}$, and $\boldsymbol{x_3} = \boldsymbol{x}^{\boldsymbol{b}}$. As discussed in Section 4.3 $F_{\mathrm{CH}_4,0}^{a,PMR}$ cannot contribute to the production of $F_{\mathrm{H}_2,ex}$ at the initial control stage,. Therefore, the expected H_2 extraction, denoted as $y_1' = F_{\mathrm{H}_2,ex,exp}$, is used as the new control target for the first subsystem. The $F_{\mathrm{H}_2,ex,exp}$ is defined as the expected H_2 extraction based on the completion of the control task of the second subsystem. Consequently, $HR(t) = HR_{sp}$ in the prediction horizons of the first subsystem is assumed, indicating an almost complete extraction. Therefore, Eq. (104):

$$y_1' = F_{\mathrm{H}_2,ex,exp} = F_{\mathrm{H}_2,max} HR_{sp} \tag{104}$$

From the PMR model, $F_{\mathrm{H}_2,ex,exp}$ can be estimated based on Eqs. (74) and (75) as follows:

$$\hat{F}_{\mathrm{H}_2,ex,exp} = (\hat{q}^{a,PMR} C_{\mathrm{H}_2}^{a,PMR} + \hat{q}^{c,PMR} \hat{C}_{\mathrm{H}_2}^{c,PMR} - F_{\mathrm{H}_2,0}^{c,PMR}) HR_{sp} \tag{105}$$

Based on this assumption, the control target of the first subsystem (y_1') can be influenced directly by the total H_2 generation, which can be governed by the $F_{\mathrm{CH}_4,0}^{a,PMR}$. At the final steady state, $y_1 = y_1' = y_{1,sp}$ since the assumption is satisfied ($HR(t) = HR_{sp}$).

A comparison between centralized MPC and decentralized MPC is illustrated in Fig. 8. The DMPC control simulation is represented by the grey curve, while the CMPC control curve is shown in purple. The behavior of the CMPC during the first hour of control is identical to that depicted in Fig. 7. In contrast, $F_{\mathrm{CH}_4,0}^{a,PMR}$ increases continuously from 20 sccm to 33.8 sccm. This behavior is attributed to the independent control action of the first subsystem that attempts to increase $F_{\mathrm{H}_2,ex,exp}$ by increasing $F_{\mathrm{CH}_4,0}^{a,PMR}$. Due to the significant increase in $F_{\mathrm{CH}_4,0}^{a,PMR}$, the furnace supplies

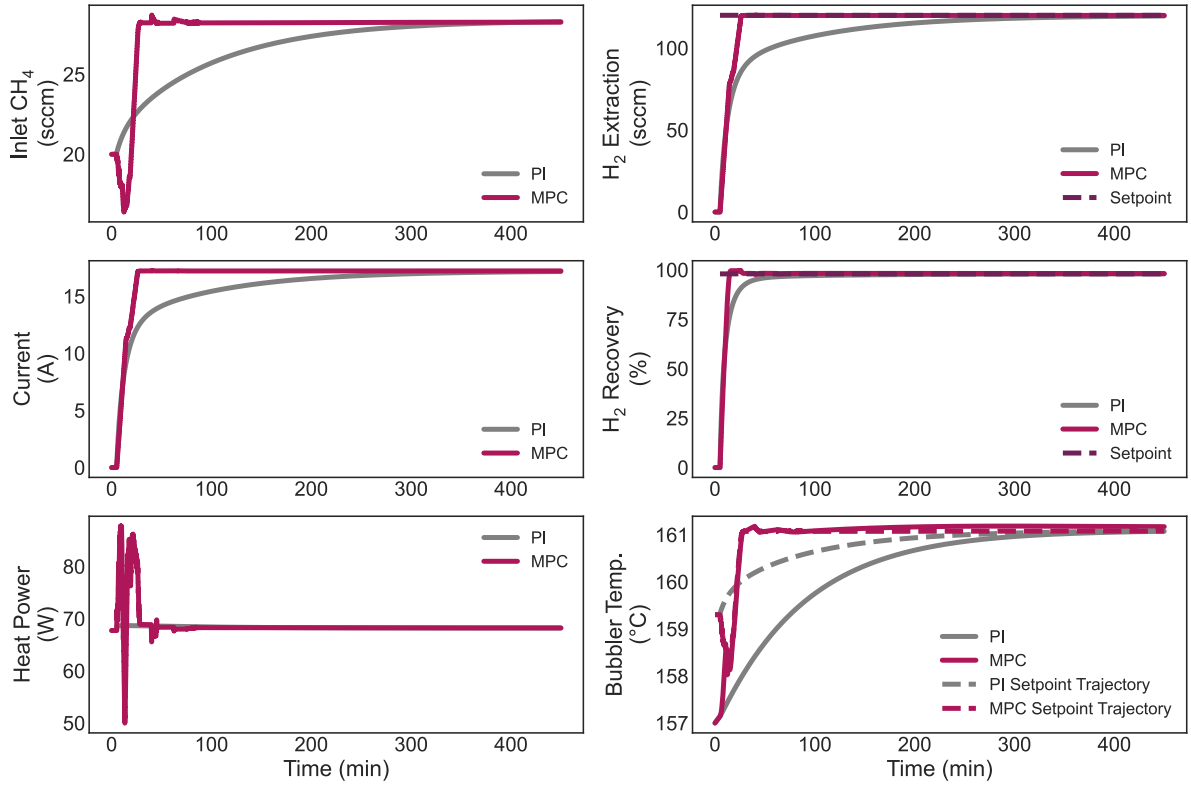

Fig. 7. Comparison of PI and MPC for the PMR system at the same inlet conditions (735 °C | 10 bar | 20 sccm CH_4) and target setpoints (HR 98% | S/C 2.5 | 120 sccm H_2 extraction). (For interpretation of the references to colour in this figure legend, the reader is referred to the web version of this article.)

more heat to the bubbler compared to the CMPC scheme. After increasing $F_{CH_4,0}^{a,PMR}$, the steam fraction inside of the bubbler must also increase to maintain the same value of S/C, as indicated in Eq. (79). The temperature setpoint of the bubbler is increased according to Eq. (78). After $F_{CH_4,0}^{a,PMR}$ reaches 33.8 sccm, a monotonic decrease of methane is shown until the extraction setpoint, $F_{H_2,ex,sp}$, is reached. The decrease in methane is caused by the gradual increase in the electric current passed through the membrane that propagates a shift in the thermodynamic equilibrium of the gas-phase reactions (Eq. (22)), allowing for greater H_2 production and thereby reducing the need for $F_{CH_4,0}^{a,PMR}$. Although the controlled process variable trajectories differ, all control outputs reach their setpoints around $t = 28$ min.

To highlight the advantages of DMPC, a detailed comparison is provided in Fig. 9. In this figure, *Computational Time* refers to the execution time required to simulate each MPC run, *Cost* refers to the value of the cost function for the centralized MPC (Eq. (3d)), and *Optimizer Failure Percentage* describes the percentage of divergence failures when solving the optimization problem for each MPC run. The comparison demonstrates that decentralized MPC significantly reduces computational time by a factor of six, though with some compromises in the controller response speed. The solution of the MPC optimization problem (whether centralized MPC or decentralized MPC) in each sampling time is dependent on the code optimization and the hardware used to carry out the computations. In the present case, the decentralized MPC control actions were calculated within the controller sampling time. Moreover, the optimizer performs more reliably due to the simplification of the optimization problem into subproblems. As seen in the *Optimizer Failure Percentage* data, the failure rate for solving the optimization problem is approximately three times higher for the centralized MPC, making DMPC a reliable alternative for real-world implementation.

4.5. State estimation and disturbance compensation

To implement MPC in experimental conditions, it is essential to consider real time feedback information. As detailed in Section 2.7.2, the measurable variables include the bubbler temperature, anodic gas flowrates, and the cathodic H_2 gas flowrate. The anodic gas flowrates are recorded every 18 min, with a 15-min delay. Therefore, an estimator is required for the MPC control scheme to estimate the complete set of state variables accurately, at high frequency. Another challenge is presented when a mismatch exists between the model and the real process due to physical disturbances that are rather unpredictable. One of the possible disturbances is membrane degradation. In the experiment, proton exchange membranes were developed by CoorsTek, Inc. Though the catalysts are fairly stable for up to 750 h of reforming reactions (Malerød-Fjeld et al., 2017), inevitably, the membrane performance will degrade over time and the electrical resistance of the closed circuit will increase, causing further performance loss for reactions and hydrogen separation.

To address unexpected disturbances, a disturbance observer-based model was formulated. The purpose of the disturbance observer is to correct for any mismatch between model predictions and real-time feedback information from the process.

For the model of the anode, according to Eqs. (7) and (45), the disturbance observer-based anode concentrations ($\dot{\tilde{\boldsymbol{C}}}^{a,PMR} = \left[\tilde{C}_{CH_4}^{a,PMR} \quad \tilde{C}_{H_2O}^{a,PMR} \quad \tilde{C}_{CO}^{a,PMR} \quad \tilde{C}_{H_2}^{a,PMR} \quad \tilde{C}_{CO_2}^{a,PMR} \quad \tilde{C}_{Ar}^{a,PMR}\right]^{\top}$) are calculated as follows.

$$\dot{\tilde{\boldsymbol{C}}}^{a,PMR} = \frac{\boldsymbol{F}_{\boldsymbol{0}}^{a,PMR} + \boldsymbol{R} - \tilde{q}^{a,PMR}\boldsymbol{C}^{a,PMR} - \boldsymbol{F}_{ex}}{V^{a,PMR}} + \boldsymbol{L}_{\boldsymbol{C}}^{a,PMR}(\boldsymbol{y} - \tilde{\boldsymbol{y}}) + \boldsymbol{B}_{d,C}^{a,PMR}\tilde{\boldsymbol{d}}_{\boldsymbol{C}}^{a,PMR} \tag{106a}$$

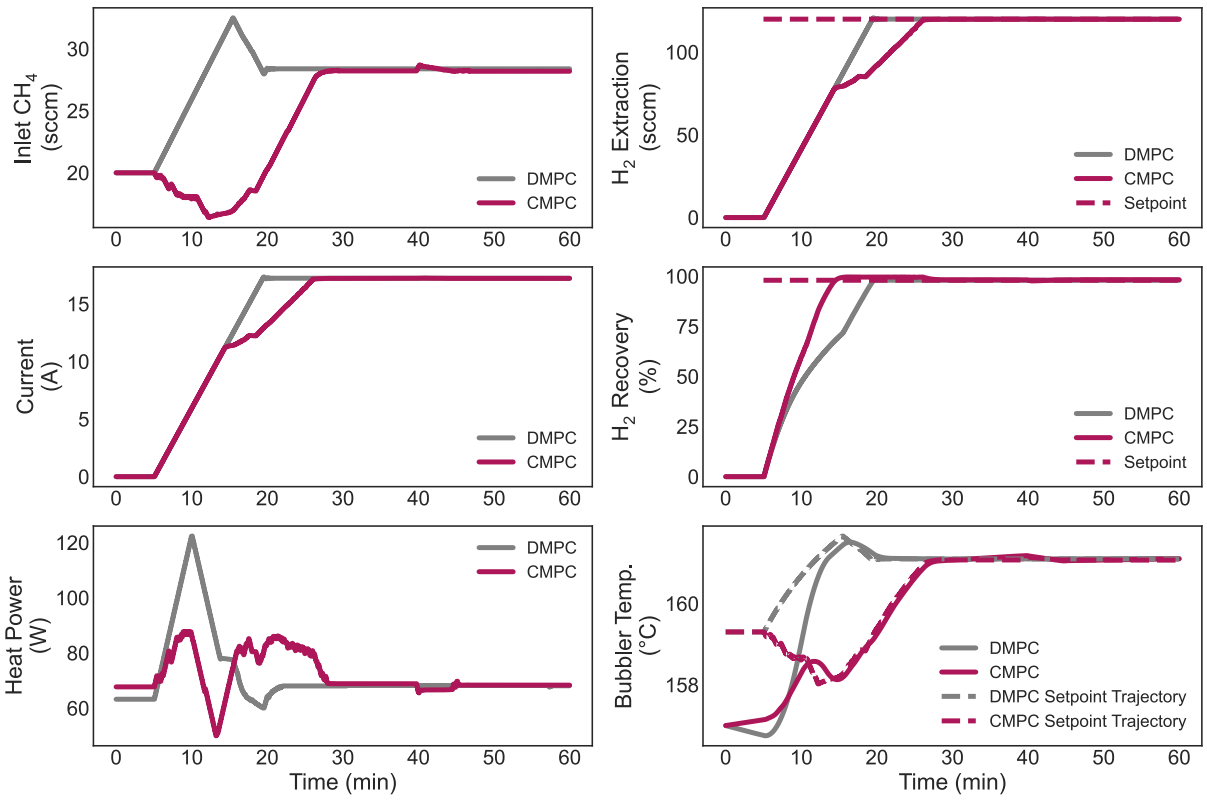

Fig. 8. Comparison of centralized MPC and decentralized MPC for the PMR system at the same inlet conditions (735 °C | 10 bar | 20 sccm CH_4) and target setpoints (HR 98% | S/C 2.5 | 120 sccm H_2 extraction). (For interpretation of the references to colour in this figure legend, the reader is referred to the web version of this article.)

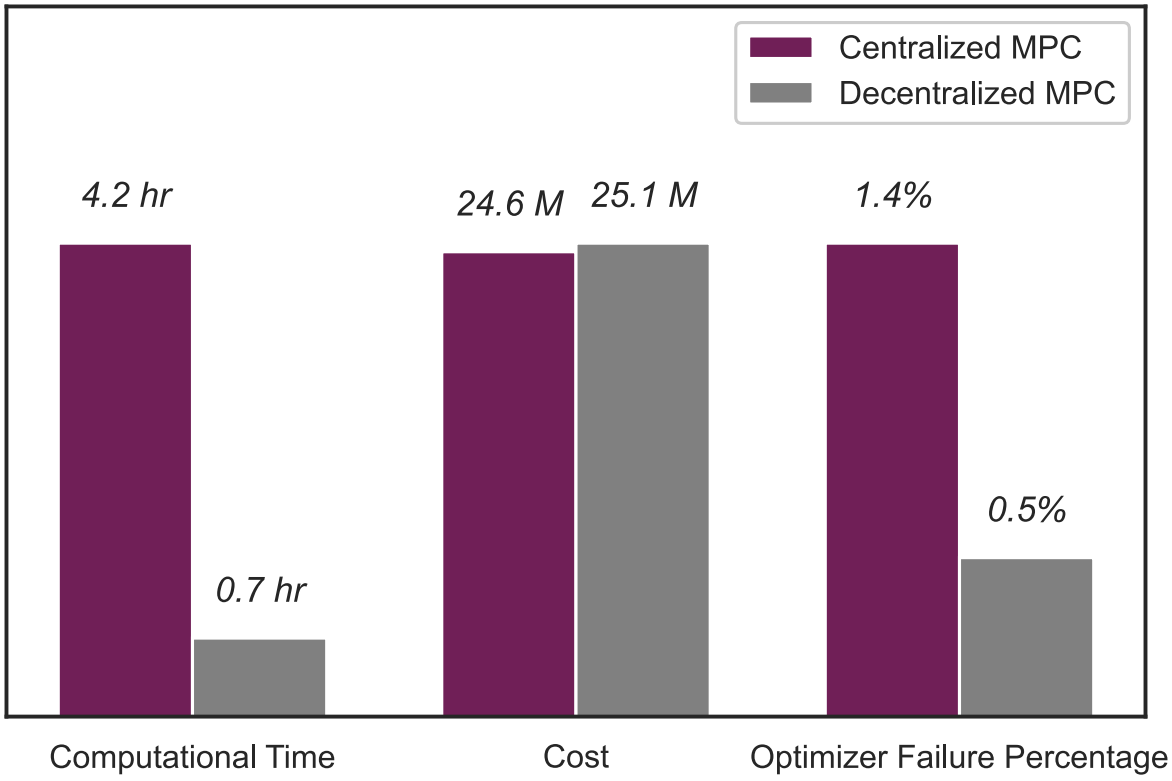

Fig. 9. Comparison of the PMR-implemented centralized MPC and decentralized MPC computational efficiencies, system energy costs, and the optimizer (software solver) reliability under both control schemes.

$$\dot{\tilde{\xi}}_C^{a,PMR} = \boldsymbol{W}_C^{a,PMR}\tilde{\xi}_C^{a,PMR} + \boldsymbol{L}_{\tilde{\xi},C}^{a,PMR}(\boldsymbol{y}-\tilde{\boldsymbol{y}}) \tag{106b}$$

$$\tilde{\boldsymbol{d}}_C^{a,PMR} = \boldsymbol{V}_C^{a,PMR}\tilde{\xi}_C^{a,PMR} \tag{106c}$$

In this equation, $\boldsymbol{F}_{\boldsymbol{0}}^{a,PMR}$, $\boldsymbol{R}$, $\boldsymbol{F}_{ex}$ are defined in Eq. (45b) and $\boldsymbol{y}$ is defined in Eq. (80). Considering the sampling time of each measurement, $\boldsymbol{y} = \begin{bmatrix} y_1 & y_2 & y_3 \end{bmatrix}^\top = \begin{bmatrix} y_1(t_{n1}) & y_2(t_{n2}) & y_3(t_{n3}) \end{bmatrix}^\top$, where t_{n1}, t_{n2}, t_{n3} are moment when real time data are received. The corresponding sampling times are $\Delta t_{n1} = 1$ s, $\Delta t_{n2} = 18$ min, $\Delta t_{n3} = 1$ s. Other vectors and matrices in Eq. (106) are defined in Eq. (107).

$$\boldsymbol{L}_C^{a,PMR} = \begin{bmatrix} L_{H_2,CH_4}^{a,PMR} & L_{HR,CH_4}^{a,PMR} & L_{T^b,CH_4}^{a,PMR} \\ L_{H_2,H_2O}^{a,PMR} & L_{HR,H_2O}^{a,PMR} & L_{T^b,H_2O}^{a,PMR} \\ L_{H_2,CO}^{a,PMR} & L_{HR,CO}^{a,PMR} & L_{T^b,CO}^{a,PMR} \\ L_{H_2,H_2}^{a,PMR} & L_{HR,H_2}^{a,PMR} & L_{T^b,H_2}^{a,PMR} \\ L_{H_2,CO_2}^{a,PMR} & L_{HR,CO_2}^{a,PMR} & L_{T^b,CO_2}^{a,PMR} \\ L_{H_2,Ar}^{a,PMR} & L_{HR,Ar}^{a,PMR} & L_{T^b,Ar}^{a,PMR} \end{bmatrix}, \quad \boldsymbol{L}_{\tilde{\xi},C}^{a,PMR} = \begin{bmatrix} L_{H_2,CH_4,\tilde{\xi}}^{a,PMR} & L_{HR,CH_4,\tilde{\xi}}^{a,PMR} & L_{T^b,CH_4,\tilde{\xi}}^{a,PMR} \\ L_{H_2,H_2O,\tilde{\xi}}^{a,PMR} & L_{HR,H_2O,\tilde{\xi}}^{a,PMR} & L_{T^b,H_2O,\tilde{\xi}}^{a,PMR} \\ L_{H_2,CO,\tilde{\xi}}^{a,PMR} & L_{HR,CO,\tilde{\xi}}^{a,PMR} & L_{T^b,CO,\tilde{\xi}}^{a,PMR} \\ L_{H_2,H_2,\tilde{\xi}}^{a,PMR} & L_{HR,H_2,\tilde{\xi}}^{a,PMR} & L_{T^b,H_2,\tilde{\xi}}^{a,PMR} \\ L_{H_2,CO_2,\tilde{\xi}}^{a,PMR} & L_{HR,CO_2,\tilde{\xi}}^{a,PMR} & L_{T^b,CO_2,\tilde{\xi}}^{a,PMR} \\ L_{H_2,Ar,\tilde{\xi}}^{a,PMR} & L_{HR,Ar,\tilde{\xi}}^{a,PMR} & L_{T^b,Ar,\tilde{\xi}}^{a,PMR} \end{bmatrix}$$

$$\tilde{\boldsymbol{y}} = \begin{bmatrix} \tilde{F}_{H_2,ex} \\ H\tilde{R} \\ \tilde{T}^b \end{bmatrix}, \quad \boldsymbol{B}_{d,C}^{a,PMR} = \begin{bmatrix} B_{d,CH_4}^{a,PMR} & 0 & 0 & 0 & 0 & 0 \\ 0 & B_{d,H_2O}^{a,PMR} & 0 & 0 & 0 & 0 \\ 0 & 0 & B_{d,CO}^{a,PMR} & 0 & 0 & 0 \\ 0 & 0 & 0 & B_{d,H_2}^{a,PMR} & 0 & 0 \\ 0 & 0 & 0 & 0 & B_{d,CO_2}^{a,PMR} & 0 \\ 0 & 0 & 0 & 0 & 0 & B_{d,Ar}^{a,PMR} \end{bmatrix}$$

$$\boldsymbol{d}_C^{a,PMR} = \begin{bmatrix} d_{CH_4}^{a,PMR} \\ d_{H_2O}^{a,PMR} \\ d_{CO}^{a,PMR} \\ d_{H_2}^{a,PMR} \\ d_{CO_2}^{a,PMR} \\ d_{Ar}^{a,PMR} \end{bmatrix}, \quad \tilde{\xi}_C^{a,PMR} = \begin{bmatrix} \tilde{\xi}_{CH_4}^{a,PMR} \\ \tilde{\xi}_{H_2O}^{a,PMR} \\ \tilde{\xi}_{CO}^{a,PMR} \\ \tilde{\xi}_{H_2}^{a,PMR} \\ \tilde{\xi}_{CO_2}^{a,PMR} \\ \tilde{\xi}_{Ar}^{a,PMR} \end{bmatrix} \tag{107}$$

$$\boldsymbol{W}_C^{a,PMR} = \begin{bmatrix} W_{CH_4}^{a,PMR} & 0 & 0 & 0 & 0 & 0 \\ 0 & W_{H_2O}^{a,PMR} & 0 & 0 & 0 & 0 \\ 0 & 0 & W_{CO}^{a,PMR} & 0 & 0 & 0 \\ 0 & 0 & 0 & W_{H_2}^{a,PMR} & 0 & 0 \\ 0 & 0 & 0 & 0 & W_{CO_2}^{a,PMR} & 0 \\ 0 & 0 & 0 & 0 & 0 & W_{Ar}^{a,PMR} \end{bmatrix}$$

$$\boldsymbol{V}_C^{a,PMR} = \begin{bmatrix} V_{CH_4}^{a,PMR} & 0 & 0 & 0 & 0 & 0 \\ 0 & V_{H_2O}^{a,PMR} & 0 & 0 & 0 & 0 \\ 0 & 0 & V_{CO}^{a,PMR} & 0 & 0 & 0 \\ 0 & 0 & 0 & V_{H_2}^{a,PMR} & 0 & 0 \\ 0 & 0 & 0 & 0 & V_{CO_2}^{a,PMR} & 0 \\ 0 & 0 & 0 & 0 & 0 & V_{Ar}^{a,PMR} \end{bmatrix}$$

Based on this modified first-order derivative of anode concentrations, the corresponding volumetric flowrate ($\tilde{q}^{a,PMR}$) expression is modified according to Eqs. (28) and (106a) to obey the ideal gas law assumption.

$$\begin{aligned} \tilde{q}^{a,PMR} = & \left(\sum F_{i,0}^{a,PMR} + 2r_1 W_{cat} - \frac{I_m}{2F_a} \right) \frac{RT^{a,PMR}}{P^{a,PMR}} + \frac{V^{a,PMR}}{\tilde{T}^{a,PMR}} \dot{\tilde{T}}^{a,PMR} \\ & + \frac{RT^{a,PMR} V^{a,PMR}}{P^{a,PMR}} \left(\sum L_{H_2,i}^{a,PMR} \left(F_{H_2,ex} - \tilde{F}_{H_2,ex} \right) + \sum L_{HR,i}^{a,PMR} \left(HR - H\tilde{R} \right) \right. \\ & \left. + \sum L_{T^b,i}^{a,PMR} \left(T^b - \tilde{T}^b \right) + \sum B_{d,ii}^{a,PMR} d_i^{a,PMR} \right) \end{aligned} \tag{108}$$

Where the $\tilde{T}^{a,PMR}$ is calculated by the modified version of the energy balance expression in the anode of the PMR. This modified version is obtained by combining Eqs. (7) and (56).

$$\dot{\tilde{T}}^{a,PMR} = \frac{f_h^{a,PMR} I_f^2 R_f + \sum F_{i,0}^{a,PMR} \int_{T_0^{a,PMR}}^{\tilde{T}^{a,PMR}} C_{p,i}\, dT' - r_1 W_{cat} \Delta H_1(\tilde{T}^{a,PMR}) - r_2 W_{cat} \Delta H_2(\tilde{T}^{a,PMR})}{\sum \rho_i^{a,PMR} C_{p,i} V^{a,PMR}}$$

$$+\frac{U_h^{a,PMR}A_h^{a,PMR}(T^a-\tilde{T}^{a,PMR})+\frac{1}{2}I_m^2R_m+\frac{I_m}{4F_a}RT^{a,PMR}\ln(\frac{P^{c,PMR}}{P^{a,PMR}})}{\sum\rho_i^{a,PMR}C_{p,i}V^{a,PMR}}+\boldsymbol{L}_{\boldsymbol{T}}^{\boldsymbol{a,PMR}}(\boldsymbol{y}-\tilde{\boldsymbol{y}})$$

$$+B_{d,T}^{a,PMR}d_T^{a,PMR} \tag{109a}$$

$$\dot{\tilde{\xi}}_T^{a,PMR}=W_T^{a,PMR}\xi_T^{a,PMR}+\boldsymbol{L}_{\tilde{\xi},\boldsymbol{T}}^{\boldsymbol{a,PMR}}(\boldsymbol{y}-\tilde{\boldsymbol{y}}) \tag{109b}$$

$$\tilde{d}_T^{a,PMR}=V_T^{a,PMR}\tilde{\xi}_T^{a,PMR} \tag{109c}$$

Where $\boldsymbol{L}_{\boldsymbol{T}}^{\boldsymbol{a,PMR}}=\begin{bmatrix}L_{\mathrm{H_2},T}^{a,PMR} & L_{HR,T}^{a,PMR} & L_{T^b,T}^{a,PMR}\end{bmatrix}^\top$ and $\boldsymbol{L}_{\boldsymbol{T,\xi}}^{\boldsymbol{a,PMR}}=\begin{bmatrix}L_{\mathrm{H_2},T,\xi}^{a,PMR} & L_{HR,T,\xi}^{a,PMR} & L_{T^b,T,\xi}^{a,PMR}\end{bmatrix}^\top$.

For the cathode, concentrations ($\tilde{\boldsymbol{C}}^{\boldsymbol{c,PMR}}=\begin{bmatrix}\tilde{C}_{\mathrm{H_2O}}^{c,PMR} & \tilde{C}_{\mathrm{H_2}}^{c,PMR}\end{bmatrix}^\top$) are estimated by combining Eq. (58) with the disturbance observer, shown as follows:

$$\dot{\tilde{\boldsymbol{C}}}^{\boldsymbol{c,PMR}}=\frac{\boldsymbol{F}_{\boldsymbol{0}}^{\boldsymbol{c,PMR}}-\tilde{q}^{c,PMR}\tilde{\boldsymbol{C}}^{\boldsymbol{c,PMR}}+\boldsymbol{F}_{ex}}{V^{c,PMR}}+\boldsymbol{L}_{\boldsymbol{C}}^{\boldsymbol{c,PMR}}(\boldsymbol{y}-\tilde{\boldsymbol{y}})+\boldsymbol{B}_{\boldsymbol{d,C}}^{\boldsymbol{c,PMR}}\tilde{\boldsymbol{d}}_{\boldsymbol{C}}^{\boldsymbol{c,PMR}} \tag{110a}$$

$$\dot{\tilde{\xi}}_{\boldsymbol{C}}^{\boldsymbol{c,PMR}}=\boldsymbol{W}_{\boldsymbol{C}}^{\boldsymbol{c,PMR}}\xi_{\boldsymbol{C}}^{\boldsymbol{c,PMR}}+\boldsymbol{L}_{\tilde{\xi},\boldsymbol{C}}^{\boldsymbol{c,PMR}}(\boldsymbol{y}-\tilde{\boldsymbol{y}}) \tag{110b}$$

$$\tilde{\boldsymbol{d}}_{\boldsymbol{C}}^{\boldsymbol{c,PMR}}=\boldsymbol{V}_{\boldsymbol{C}}^{\boldsymbol{c,PMR}}\xi_{\boldsymbol{C}}^{\boldsymbol{c,PMR}} \tag{110c}$$

where $\boldsymbol{F}_{\boldsymbol{0}}^{\boldsymbol{c,PMR}}$, $\boldsymbol{F}_{ex}$ are defined in Eq. (34b) and $\boldsymbol{y}$ is defined in Eq. (80). Both sets of the disturbance observer-related vectors are defined in Eqs. (107) and (111).

$$\begin{aligned}
\boldsymbol{L}_{\boldsymbol{C}}^{\boldsymbol{c,PMR}}&=\begin{bmatrix}L_{\mathrm{H_2,H_2O}}^{c,PMR} & L_{HR,\mathrm{H_2O}}^{c,PMR} & L_{T^b,\mathrm{H_2O}}^{a,PMR}\\ L_{\mathrm{H_2,H_2}}^{a,PMR} & L_{HR,\mathrm{H_2}}^{a,PMR} & L_{T^b,\mathrm{H_2}}^{a,PMR}\end{bmatrix},\quad \boldsymbol{L}_{\tilde{\boldsymbol{\xi}},\boldsymbol{C}}^{\boldsymbol{a,PMR}}=\begin{bmatrix}L_{\mathrm{H_2,H_2O},\tilde{\xi}}^{a,PMR} & L_{HR,\mathrm{H_2O},\tilde{\xi}}^{a,PMR} & L_{T^b,\mathrm{H_2O},\tilde{\xi}}^{a,PMR}\\ L_{\mathrm{H_2,H_2},\tilde{\xi}}^{a,PMR} & L_{HR,\mathrm{H_2},\tilde{\xi}}^{a,PMR} & L_{T^b,\mathrm{H_2},\tilde{\xi}}^{a,PMR}\end{bmatrix}\\
\tilde{\boldsymbol{y}}&=\begin{bmatrix}\tilde{F}_{\mathrm{H_2},ex}\\ \tilde{HR}\\ \tilde{T}^b\end{bmatrix},\quad \boldsymbol{B}_{\boldsymbol{d,C}}^{\boldsymbol{c,PMR}}=\begin{bmatrix}B_{d,\mathrm{H_2O}}^{c,PMR} & 0\\ 0 & B_{d,\mathrm{H_2}}^{c,PMR}\end{bmatrix},\quad \tilde{\boldsymbol{d}}_{\boldsymbol{C}}^{\boldsymbol{c,PMR}}=\begin{bmatrix}d_{\mathrm{H_2O}}^{c,PMR}\\ d_{\mathrm{H_2}}^{c,PMR}\end{bmatrix}\\
\tilde{\boldsymbol{\xi}}_{\boldsymbol{C}}^{\boldsymbol{c,PMR}}&=\begin{bmatrix}\tilde{\xi}_{\mathrm{H_2O}}^{c,PMR}\\ \tilde{\xi}_{\mathrm{H_2}}^{c,PMR}\end{bmatrix},\quad \boldsymbol{W}_{\boldsymbol{C}}^{\boldsymbol{c,PMR}}=\begin{bmatrix}W_{\mathrm{H_2O}}^{c,PMR} & 0\\ 0 & W_{\mathrm{H_2}}^{c,PMR}\end{bmatrix},\quad \boldsymbol{V}_{\boldsymbol{C}}^{\boldsymbol{c,PMR}}=\begin{bmatrix}V_{\mathrm{H_2O}}^{c,PMR} & 0\\ 0 & V_{\mathrm{H_2}}^{c,PMR}\end{bmatrix}
\end{aligned} \tag{111}$$

Based on this modified first-order derivative of cathode concentrations, the volumetric flowrate ($\tilde{q}^{c,PMR}$) expression is modified according to Eqs. (28) and (110a) to obey the ideal gas law assumption.

$$\begin{aligned}
\tilde{q}^{c,PMR}=&\left(\sum F_{i,0}^{c,PMR}+\frac{I_m}{2F_a}\right)\frac{R\tilde{T}^{c,PMR}}{P^{c,PMR}}+\frac{V^{c,PMR}}{\tilde{T}^{c,PMR}}\dot{\tilde{T}}^{c,PMR}+V^{c,PMR}\left(\sum L_{\mathrm{H_2},i}^{c,PMR}(F_{\mathrm{H_2},ex}-\tilde{F}_{\mathrm{H_2},ex})\right.\\
&\left.+\sum L_{HR,i}^{c,PMR}(HR-\tilde{HR})+\sum L_{T^b,i}^{c,PMR}(T^b-\tilde{T}^b)+\sum B_{d,i}^{c,PMR}d_i^{c,PMR}\right)\frac{R\tilde{T}^{c,PMR}}{P^{c,PMR}}
\end{aligned} \tag{112}$$

Where the $\tilde{T}^{c,PMR}$ is calculated by the modified version of the energy balance expression in the cathode side of PMR. This modified version is obtained by combining Eqs. (7) and (59).

$$\dot{\tilde{T}}^{c,PMR}=\frac{f_h^{c,PMR}I_f^2R_f+\sum F_{i,0}^{c,PMR}\int_{T_0^{c,PMR}}^{T^{c,PMR}}C_{p,i}\,dT'+\frac{I_m}{2F_a}\int_{T^{a,PMR}}^{T^{c,PMR}}C_{p,\mathrm{H_2}}\,dT'}{\sum\rho_i^{c,PMR}C_{p,i}V^{c,PMR}}$$

$$+\frac{U_h^{c,PMR}A_h^{c,PMR}(T^a-T^{c,PMR})+\frac{1}{2}I_m^2R_m+\frac{I_m}{4F_a}RT^{c,PMR}\ln(\frac{P^{c,PMR}}{P^{a,PMR}})}{\sum\rho_i^{c,PMR}C_{p,i}V^{c,PMR}}+\boldsymbol{L}_{\boldsymbol{T}}^{\boldsymbol{c,PMR}}(\boldsymbol{y}-\tilde{\boldsymbol{y}})$$

$$+B_{d,T}^{c,PMR}d_T^{c,PMR} \tag{113a}$$

$$\dot{\tilde{\xi}}_T^{c,PMR}=W_T^{c,PMR}\xi_T^{c,PMR}+\boldsymbol{L}_{\tilde{\xi},\boldsymbol{T}}^{\boldsymbol{c,PMR}}(\boldsymbol{y}-\tilde{\boldsymbol{y}}) \tag{113b}$$

$$\tilde{d}_T^{c,PMR}=V_T^{c,PMR}\xi_T^{c,PMR} \tag{113c}$$

Therefore, for the PMR process, the estimated state vector is defined as

$$\tilde{\boldsymbol{x}}^{\boldsymbol{PMR}}=\begin{bmatrix}\tilde{\boldsymbol{C}}^{\boldsymbol{a,PMR}}\\ \tilde{T}^{a,PMR}\\ \tilde{\boldsymbol{C}}^{\boldsymbol{c,PMR}}\\ \tilde{T}^{c,PMR}\end{bmatrix} \tag{114}$$

The bubbler model ($\tilde{\boldsymbol{x}}^{\boldsymbol{b}}=\begin{bmatrix}\tilde{T}^b & \tilde{N}_{\mathrm{H_2O},L}\end{bmatrix}^\top$) is also augmented with the additional disturbance observer terms, shown as

$$\dot{\tilde{\boldsymbol{x}}}^{\boldsymbol{b}}=\tilde{\boldsymbol{F}}(\tilde{\boldsymbol{x}}^{\boldsymbol{b}},\boldsymbol{u})+\boldsymbol{L}^{\boldsymbol{b}}(\boldsymbol{y}-\tilde{\boldsymbol{y}})+\boldsymbol{B}_{\boldsymbol{d}}^{\boldsymbol{b}}\tilde{\boldsymbol{d}}^{\boldsymbol{b}} \tag{115a}$$

$$\dot{\tilde{\boldsymbol{\xi}}}^{\boldsymbol{b}}=\boldsymbol{w}^{\boldsymbol{b}}\tilde{\boldsymbol{\xi}}^{\boldsymbol{b}}+\boldsymbol{L}_{\tilde{\boldsymbol{\xi}}}^{\boldsymbol{b}}(\boldsymbol{y}-\tilde{\boldsymbol{y}}) \tag{115b}$$

$$\tilde{\boldsymbol{d}}^{\boldsymbol{b}}=\boldsymbol{v}^{\boldsymbol{b}}\tilde{\boldsymbol{\xi}}^{\boldsymbol{b}} \tag{115c}$$

Where corresponding vectors are defined as:

$$\tilde{\boldsymbol{F}}(\tilde{\boldsymbol{x}}^{\boldsymbol{b}},\boldsymbol{u})=\begin{bmatrix}\dfrac{\dot{Q}^b-\sum F^b_{i,0}\int_{T^b_0}^{\tilde{T}^b}C_{p,i}dT'+U^bA^b(T^a-\tilde{T}^b)}{\tilde{N}^b_{\mathrm{H_2O},L}M_{\mathrm{H_2O}}C_{p,\mathrm{H_2O}}+V^b_{gas}\sum\rho^b_jC_{p,j}}\\ \dfrac{\left(\frac{\tilde{N}_{\mathrm{H_2O},L}M_{\mathrm{H_2O}}}{R\rho_{\mathrm{H_2O}}}-\frac{V^b}{R}\right)\dot{\lambda}^b-\frac{P^b_s\sum F^b_{i,0}}{P^b-P^b_s}}{1-\frac{P^b_sM_{\mathrm{H_2O}}}{R\tilde{T}^b\rho_{\mathrm{H_2O}}}}\end{bmatrix},\quad \boldsymbol{L^b}=\begin{bmatrix}L^b_{\mathrm{H_2},\tilde{T}^b} & L^b_{HR,\tilde{T}^b} & L^b_{T^b,\tilde{T}^b}\\ L^b_{\mathrm{H_2},\tilde{N}_{\mathrm{H_2O},L}} & L^b_{HR,\tilde{N}_{\mathrm{H_2O},L}} & L^b_{T^b,\tilde{N}_{\mathrm{H_2O},L}}\end{bmatrix} \tag{116a}$$

$$\boldsymbol{B^b_d}=\begin{bmatrix}B^b_{d,\tilde{T}^b} & 0\\ 0 & B^b_{d,\tilde{N}_{\mathrm{H_2O},L}}\end{bmatrix},\quad \tilde{\boldsymbol{d}}^{\boldsymbol{b}}=\begin{bmatrix}d^b_{\tilde{T}^b}\\ d^b_{\tilde{N}_{\mathrm{H_2O},L}}\end{bmatrix},\quad \tilde{\boldsymbol{\xi}}^{\boldsymbol{b}}=\begin{bmatrix}\tilde{\xi}^b_{\tilde{T}^b}\\ \tilde{\xi}^b_{\tilde{N}_{\mathrm{H_2O}}}\end{bmatrix}$$

$$\boldsymbol{w^b}=\begin{bmatrix}w^b_{\tilde{T}^b} & 0\\ 0 & w^b_{\tilde{N}_{\mathrm{H_2O}}}\end{bmatrix},\quad \boldsymbol{L^b_{\tilde{\xi}}}=\begin{bmatrix}L^b_{\mathrm{H_2},\tilde{\xi},\tilde{T}^b} & L^b_{HR,\tilde{\xi},\tilde{T}^b} & L^b_{T^b,\tilde{\xi},\tilde{T}^b}\\ L^b_{\mathrm{H_2},\tilde{\xi},\tilde{N}_{\mathrm{H_2O}}} & L^b_{HR,\tilde{\xi},\tilde{N}_{\mathrm{H_2O}}} & L^b_{T^b,\tilde{\xi},\tilde{N}_{\mathrm{H_2O}}}\end{bmatrix}$$

$$\boldsymbol{v^b}=\begin{bmatrix}v^b_{\tilde{T}^b} & 0\\ 0 & v^b_{\tilde{N}_{\mathrm{H_2O}}}\end{bmatrix} \tag{116b}$$

Therefore, the overall disturbance observer-based state variables can be summarized as follows:

$$\tilde{\boldsymbol{x}}=\begin{bmatrix}\tilde{\boldsymbol{x}}^{\boldsymbol{PMR}}\\ \tilde{\boldsymbol{x}}^{\boldsymbol{b}}\\ \tilde{\boldsymbol{\xi}}^{\boldsymbol{PMR}}\\ \tilde{\boldsymbol{\xi}}^{\boldsymbol{b}}\end{bmatrix} \tag{117}$$

Since the feasible region of current (U_2) is derived from the developed model, U_2 should be modified accordingly as U_2'. To satisfy Eq. (85a), the following should be held:

$$I_m(t)\le I'_{m,max,1}(t) \tag{118a}$$

$$\begin{aligned}I'_{m,max,1}(t)=2F_a\Bigg(&\sum F^{a,PMR}_{i,0}(t)+2r_1(t)W_{cat}+\frac{P^{a,PMR}V^{a,PMR}}{R\left(T^{a,PMR}(t)\right)^2}\dot{T}^{a,PMR}(t)\\&+V^{a,PMR}\Bigg(\sum L^{a,PMR}_{\mathrm{H_2},i}\left(F_{\mathrm{H_2},ex}(t_{n1})-\tilde{F}_{\mathrm{H_2},ex}(t)\right)+\sum L^{a,PMR}_{HR,i}\left(HR(t_{n2})-\tilde{HR}(t)\right)\\&+\sum L^{c,PMR}_{T^b,i}\left(T^b(t_{n3})-\tilde{T}^b(t)\right)+\sum B_{d,i}d_i(t)\Bigg)\Bigg)\end{aligned} \tag{118b}$$

The satisfaction of Eq. (85a) by the constraint shown in Eq. (118) is demonstrated by considering Eqs. (108) and (118),

$$\begin{aligned}\tilde{q}^{a,PMR}(t)=&\frac{\sum F^{a,PMR}_{i,0}(t)+2r_1(t)W_{cat}-\frac{I_m(t)}{2F_a}}{\frac{P^{a,PMR}}{RT^{a,PMR}(t)}}+\frac{V^{a,PMR}}{\tilde{T}^{a,PMR}(t)}\dot{\tilde{T}}^{a,PMR}(t)\\&+V^{a,PMR}\Bigg(\sum L^{a,PMR}_{\mathrm{H_2},i}\left(F_{\mathrm{H_2},ex}(t_{n1})-\tilde{F}_{\mathrm{H_2},ex}(t)\right)+\sum L^{a,PMR}_{HR,i}\left(HR(t_{n2})-\tilde{HR}(t)\right)\\&+\sum L^{a,PMR}_{T^b,i}\left(T^b(t_{n3})-\tilde{T}^b(t)\right)+\sum B^{a,PMR}_{d,ii}d^{a,PMR}_i(t)\Bigg)\\\ge&\frac{\sum F^{a,PMR}_{i,0}(t)+2r_1(t)W_{cat}-\frac{I'_{m,max,1}(t)}{2F_a}}{\frac{P^{a,PMR}}{RT^{a,PMR}(t)}}+\frac{V^{a,PMR}}{\tilde{T}^{a,PMR}(t)}\dot{\tilde{T}}^{a,PMR}(t)\\&+V_{a,PMR}\Bigg(\sum L^{a,PMR}_{\mathrm{H_2},i}\left(F_{\mathrm{H_2},ex}(t_{n1})-\tilde{F}_{\mathrm{H_2},ex}(t)\right)+\sum L^{a,PMR}_{HR,i}\left(HR(t_{n2})-\tilde{HR}(t)\right)\\&+\sum L^{a,PMR}_{T^b,i}\left(T^b(t_{n3})-\tilde{T}^b(t)\right)+\sum B^{a,PMR}_{d,ii}d^{a,PMR}_i(t)\Bigg)=0\end{aligned} \tag{119}$$

To ensure Eq. (85b), the constraint shown in Eq. (99c) is modified:

$$I_m(t)\le I'_{m,max,2}(t) \tag{120a}$$

$$\begin{aligned}I'_{m,max,2}(t)=&2F_a\Bigg(F^{a,PMR}_{\mathrm{H_2},0}(t)+(3r_1(t)+r_2(t))W_{cat}+V^{a,PMR}\Bigg(L^{a,PMR}_{\mathrm{H_2},\mathrm{H_2}}(F_{\mathrm{H_2},ex}(t_{n1})-\tilde{F}_{\mathrm{H_2},ex}(t))\\&+L^{a,PMR}_{HR,\mathrm{H_2}}\left(HR(t_{n2})-\tilde{HR}(t)\right)+L^{a,PMR}_{T^b,\mathrm{H_2}}\left(T^b(t_{n3})-\tilde{T}^b(t)\right)+B^{a,PMR}_{d,\mathrm{H_2}}d^{a,PMR}_{\mathrm{H_2}}(t)\Bigg)\Bigg)\end{aligned} \tag{120b}$$

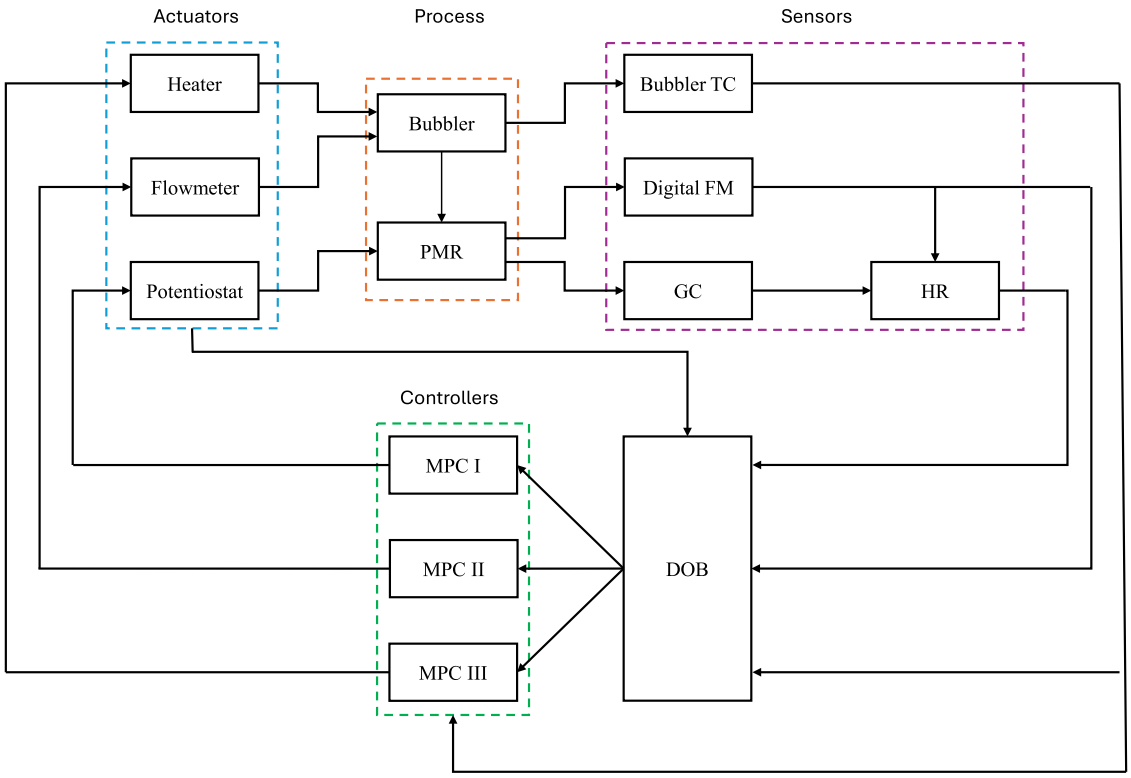

Fig. 10. Closed-loop structure of multi-input multi-output decentralized MPC control system.

The feasibility of Eq. (120) is shown by considering Eqs. (106) and (120).

$$\begin{aligned}\dot{\tilde{C}}^{a,PMR}_{H_2}(t) =& \frac{F^{a,PMR}_{H_2,0} + \left(3r_1(t) + r_2(t)\right) W_{cat} - \tilde{q}^{a,PMR}(t)\,\tilde{C}^{a,PMR}_{H_2}(t) - \frac{I_m(t)}{2F_a}}{V^{a,PMR}} \\ &+ L^{a,PMR}_{H_2,H_2}\left(F_{H_2,ex}(t_{n1}) - \tilde{F}_{H_2,ex}(t)\right) + L^{a,PMR}_{HR,H_2}\left(HR(t_{n2}) - \tilde{HR}(t)\right) \\ &+ L^{a,PMR}_{T^b,H_2}\left(T^b(t_{n3}) - \tilde{T}^b(t)\right) + B^{a,PMR}_{d,H_2} d^{a,PMR}_{H_2}(t) \\ \geq& \frac{F^{a,PMR}_{H_2,0} + \left(3r_1(t) + r_2(t)\right) W_{cat} - \tilde{q}^{a,PMR}(t)\,\tilde{C}^{a,PMR}_{H_2}(t) - \frac{I'_{m,max,2}(t)}{2F_a}}{V^{a,PMR}} \\ &+ L^{a,PMR}_{H_2,H_2}\left(F_{H_2,ex}(t_{n1}) - \tilde{F}_{H_2,ex}(t)\right) + L^{a,PMR}_{HR,H_2}\left(HR(t_{n2}) - \tilde{HR}(t)\right) \\ &+ L^{a,PMR}_{T^b,H_2}\left(T^b(t_{n3}) - \tilde{T}^b(t)\right) + B^{a,PMR}_{d,H_2} d^{a,PMR}_{H_2}(t) \\ =& -\frac{\tilde{q}^{a,PMR}(t)\,\tilde{C}^{a,PMR}_{H_2}(t)}{V^{a,PMR}}\end{aligned} \tag{121}$$

After rearranging Eq. (121), this inequality can be written as:

$$\frac{\tilde{q}^{a,PMR}(t)\,\tilde{C}^{a,PMR}_{H_2}(t)}{V^{a,PMR}} + \dot{\tilde{C}}^{a,PMR}_{H_2}(t) \geq 0 \tag{122}$$

This inequality is the same type of ODE shown in Eq. (91). Therefore, Eq. (85b) can be derived by following the steps shown in Eqs. (92)–(98).

Therefore, the modified feasible region for the electric current (U'_2) is defined as follows:

$$U'_2 = \left\{ I_m(t) \,\middle|\, 0 \leq I_m(t) \leq \min\left\{ I'_{m,max,1}(t),\ I'_{m,max,2}(t) \right\},\quad \forall t \in [0,\infty) \right\} \tag{123}$$

The closed-loop control schematic is illustrated in Fig. 10. All measurable parameters are transformed into the control target vector ($\boldsymbol{y}$) and used in the DOB-based model, developed from the error between the estimated and measured feedback ($\boldsymbol{y} - \tilde{\boldsymbol{y}}$). The DOB-based model computes all unknown state variables required as initial conditions, and the values of the input reference setpoint vector ($\boldsymbol{u_{sp}}$ in Eq. (4d)) are adaptively estimated using Eq. (10). These estimated values are then used in decentralized predictive controllers.

To test the disturbance observer design in a decentralized MPC strategy, many disturbances are added to the simulated process. The first added disturbance increases the reaction activation energies by 5% (Eq. (22)) to simulate a catalyst deactivation process initiated by solid carbon formation on the catalyst. A 1% higher heat loss term is also added to disturb the temperature of the bubbler ($U^b_h A^b_h (T^a - T^b)$ in Eq. (63)) to simulate heat insulation degradation. A third disturbance provides a 60% increase to the inlet H_2 flowrate ($F^{a,PMR}_{H_2,0}$) to simulate volumetric and concentration fluctuations to the inlet gas mixture of the PMR.

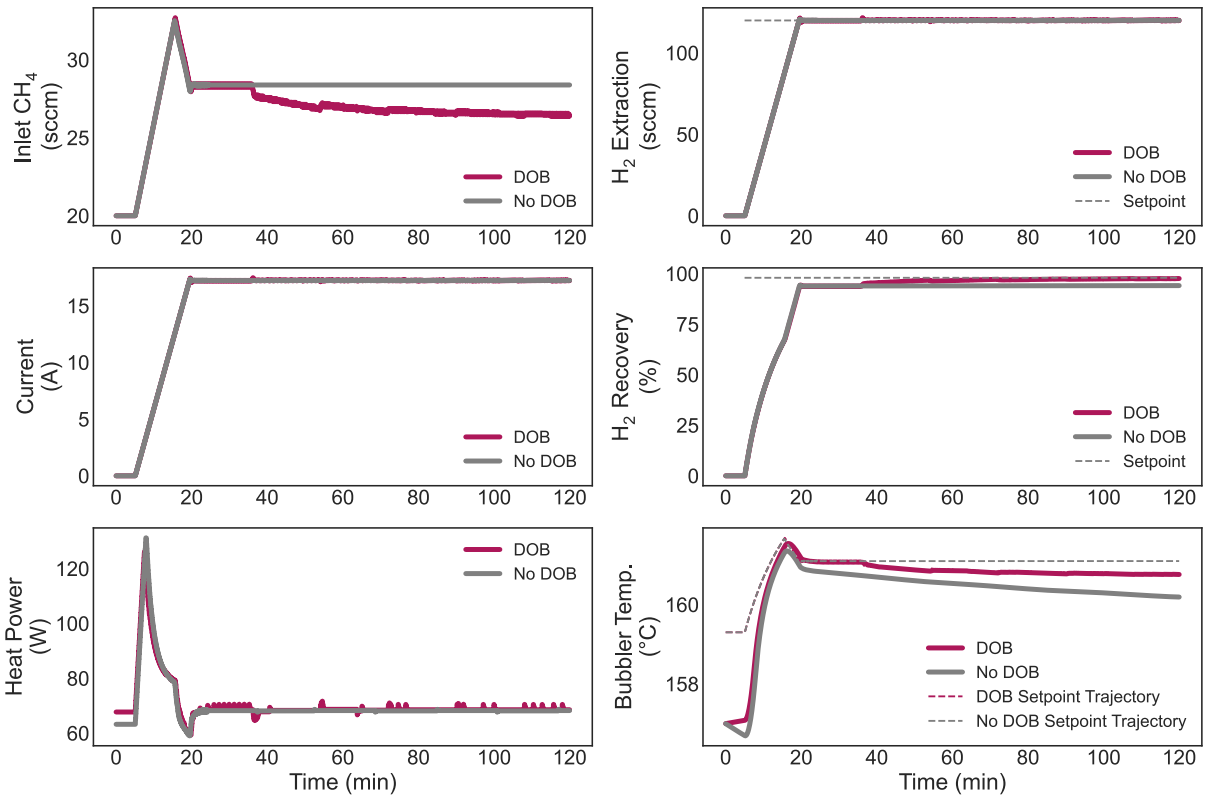

Fig. 11. Model predictive control with the disturbance observer versus without the disturbance observer at the same PMR inlet conditions (735 °C | 10 bar | 20 sccm CH_4) and target setpoints (HR 98% | S/C 2.5 | 120 sccm H_2 extraction).

The effectiveness of this control strategy is demonstrated by comparing its performance to a DMPC scheme without a DOB for model correction, shown in Fig. 11. In the figure, the grey curve represents the scenario without DOB implementation. While the H_2 extraction rate reaches the target setpoint under three types of disturbance, as the removal rate of H_2 is solely governed by Eq. (40), both HR and the bubbler temperature fail to reach their respective setpoints. The deviation from the HR target setpoint for the controllers is caused by the lack of a DOB to correct for the decrease in catalytic performance. Additionally, changes in heat loss are not incorporated into the energy balance of the original PMR model, so the model underestimates heat loss and overestimates the bubbler temperature. In contrast, when a DOB is applied to the DMPC scheme, the target setpoints are successfully reached for all three control outputs, as the model and $\boldsymbol{u}_{sp}$ are adaptively corrected over time. This adaptive correction enables the model to account for disturbances progressively, providing more accurate initial conditions for the MPC and allowing for more accurate predictions within the MPC horizons.

Remark 7. For frequent and measurable state variables, state estimation is not needed. Therefore, in this case, the measured bubbler temperature is directly utilized as the initial condition of the MPC without estimation.

5. Conclusion

In this work, a lumped-parameter model was developed for a general CST-MR system and specifically applied to a PMR system. The model was validated using experimental data, confirming its accuracy. Additionally, a lumped-parameter model was constructed for a general bubbler. Building on these models, setpoint tracking control for the PMR system was implemented to regulate key parameters relevant to real-world H_2 production processes. The MPC approach was successfully applied, incorporating system constraints and demonstrating faster response times compared to a traditional PI control strategy. A comprehensive comparison between DMPC and CMPC highlighted the effectiveness of DMPC in significantly reducing computational costs. Moreover, the disturbance observer-based decentralized MPC, utilizing the developed disturbance observer model, efficiently estimated the missing state variables and addressed common disturbances in the PMR system. The experimental implementation of the developed control strategy will be presented in a subsequent work.

CRediT authorship contribution statement

Xiaodong Cui: Writing – original draft, Methodology, Investigation, Conceptualization. **Dominic Peters:** Writing – original draft, Methodology, Investigation, Conceptualization. **Yifei Wang:** Methodology, Investigation. **Berkay Çıtmacı:** Investigation. **Derek Richard:** Writing – original draft, Investigation, Data curation. **Carlos G. Morales-Guio:** Writing – original draft, Methodology, Investigation, Conceptualization. **Panagiotis D. Christofides:** Writing – review & editing, Writing – original draft, Supervision, Conceptualization.

Declaration of competing interest

The authors declare that they have no known competing financial interests or personal relationships that could have appeared to influence the work reported in this paper.

The corresponding author, Panagiotis Christofides is an editor for the journal Chemical Engineering Research and Design, but has had no access to, or involvement in, the peer review process for this paper or its handling by the journal at any point.

Acknowledgments

We would like to gratefully acknowledge financial support from the U.S. Department of Energy, through the Office of Energy Efficiency and Renewable Energy (EERE), under the Advanced Manufacturing Office, United States Award Number DE-EE0007613. We also extend our sincere gratitude to CoorsTek, Inc. for providing the BCZY proton conducting membranes used to construct the proton membrane reformer unit for this work.

References

Abdalah, M., 2020. Modeling reactor-focused energy balances for multi-stage CSTR anaerobic digestion systems. J. Renew. Sustain. Energy 12 (6).
Barbieri, G., 2015. Continuous stirred tank membrane reactor (CST-MR). In: Drioli, E., Giorno, L. (Eds.), Encyclopedia of Membranes. Springer-Verlag GmbH.
Bemporad, A., Barcelli, D., 2010. Decentralized model predictive control. Netw. Control Syst. 149–178.
Boggs, P.T., Tolle, J.W., 1995. Sequential quadratic programming. Acta Numer. 4, 1–51.
Chen, J., Patton, R.J., Zhang, H.-Y., 1996. Design of unknown input observers and robust fault detection filters. Internat. J. Control 63 (1), 85–105.
Chen, S., Wu, Z., Christofides, P.D., 2020. Decentralized machine-learning-based predictive control of nonlinear processes. Chem. Eng. Res. Des. 162, 45–60.
Chen, W.-H., Yang, J., Guo, L., Li, S., 2015. Disturbance-observer-based control and related methods—An overview. IEEE Trans. Ind. Electron. 63 (2), 1083–1095.
Çıtmacı, B., Peters, D., Cui, X., Abdullah, F., Almunaifi, A., Chheda, P., Morales-Guio, C.G., Christofides, P.D., 2024. Feedback control of an experimental electrically-heated steam methane reformer. Chem. Eng. Res. Des. 206, 469–488.
Cui, X., Çıtmacı, B., Peters, D., Abdullah, F., Wang, Y., Hsu, E., Chheda, P., Morales-Guio, C.G., Christofides, P.D., 2024. Estimation-based model predictive control of an electrically-heated steam methane reforming process. Digit. Chem. Eng. 11, 100153.
Hsu, E., Peters, D., Çıtmacı, B., Chheda, P., Cui, X., Wang, Y., Morales-Guio, C.G., Christofides, P.D., 2024. Modeling and design of a combined electrified steam methane reforming-pressure swing adsorption process. Chem. Eng. Res. Des. 209, 111–131.
Jang, I., S. A. Carneiro, J., Crawford, J.O., Cho, Y.J., Parvin, S., Gonzalez-Casamachin, D.A., Baltrusaitis, J., Lively, R.P., Nikolla, E., 2024. Electrocatalysis in solid oxide fuel cells and electrolyzers. Chem. Rev. 124 (13), 8233–8306.
Jeon, J., Nam, S., Ko, C.H., 2018. Rapid evaluation of coke resistance in catalysts for methane reforming using low steam-to-carbon ratio. Catal. Today 309, 140–146.
Johnson, C., 1970. Further study of the linear regulator with disturbances–the case of vector disturbances satisfying a linear differential equation. IEEE Trans. Autom. Control 15 (2), 222–228.
Khamsi, M.A., Kirk, W.A., 2011. An Introduction to Metric Spaces and Fixed Point Theory. John Wiley & Sons.
Maeder, U., Borrelli, F., Morari, M., 2009. Linear offset-free model predictive control. Automatica 45 (10), 2214–2222.
Malerød-Fjeld, H., Clark, D., Yuste-Tirados, I., Zanón, R., Catalán-Martinez, D., Beeaff, D., Morejudo, S.H., Vestre, P.K., Norby, T., Haugsrud, R., et al., 2017. Thermo-electrochemical production of compressed hydrogen from methane with near-zero energy loss. Nat. Energy 2 (12), 923–931.
Meloni, E., Martino, M., Palma, V., 2020. A short review on Ni based catalysts and related engineering issues for methane steam reforming. Catal. 10, 352.
Molburg, J.C., Doctor, R.D., 2003. Hydrogen from steam-methane reforming with CO_2 capture. In: Proceedings of 20th Annual International Pittsburgh Coal Conference. Pittsburgh, PA, USA, pp. 1–21.
Richards, A., How, J., 2004. A decentralized algorithm for robust constrained model predictive control. In: Proceedings of the 2004 American Control Conference. Vol. 5, Boston, MA, USA, pp. 4261–4266.
Shomate, C.H., 1944. High-temperature heat contents of magnesium nitrate, calcium nitrate and barium nitrate1. J. Am. Chem. Soc. 66 (6), 928–929.
Soroush, M., 1997. Nonlinear state-observer design with application to reactors. Chem. Eng. Sci. 52 (3), 387–404.
Taji, M., Farsi, M., Keshavarz, P., 2018. Real time optimization of steam reforming of methane in an industrial hydrogen plant. Int. J. Hydrog. Energy 43 (29), 13110–13121.
Thomson, G.W., 1946. The antoine equation for vapor-pressure data.. Chem. Rev. 38 (1), 1–39.
Wallace, M., Pon Kumar, S.S., Mhaskar, P., 2016. Offset-free model predictive control with explicit performance specification. Ind. Eng. Chem. Res. 55 (4), 995–1003.
Wang, Y., Cui, X., Peters, D., Çıtmacı, B., Alnajdi, A., Morales-Guio, C.G., Christofides, P.D., 2024. Machine learning-based predictive control of an electrically-heated steam methane reforming process. Digit. Chem. Eng. 12, 100173.
Wrubel, J.A., Gifford, J., Ma, Z., Ding, H., Ding, D., Zhu, T., 2021. Modeling the performance and faradaic efficiency of solid oxide electrolysis cells using doped barium zirconate perovskite electrolytes. Int. J. Hydrog. Energy 46 (21), 11511–11522.
Xu, J., Froment, G.F., 1989. Methane steam reforming, methanation and water-gas shift: I. Intrinsic kinetics. AIChE J. 35 (1), 88–96.
Yuste-Tirados, I., Liu, X., Kjølseth, C., Norby, T., 2023. Impedance of a tubular electrochemical cell with BZCY electrolyte and Ni-BZCY cermet electrodes for proton ceramic membrane reactors. Int. J. Hydrog. Energy 48 (77), 30027–30038.
Yuste-Tirados, I., Liu, X., Kjølseth, C., Norby, T., 2024. Boundaries of DC operation of a tubular proton ceramic electrochemical reactor with BZCY electrolyte and Ni-BZCY cermet electrodes. J. Power Sources 596, 234097.